THESIS FOR THE DEGREE OF DOCTOR OF TECHNOLOGY IN NATURAL SCIENCE, WITH FOCUS ON CHEMISTRY

Energy efficiency in the sodium chlorate process

From electrocatalysis to pilot plant investigations

Kristoffer Hedenstedt
Department of Chemistry and Molecular Biology
Faculty of Science

ISBN 978-91-629-0103-5 (print)
ISBN 978-91-629-0104-2 (PDF)
Available online at: http://handle.net/2077/52081

UNIVERSITY OF GOTHENBURG

DEPARTMENT OF CHEMISTRY AND MOLECULAR BIOLOGY

Energy efficiency in the sodium chlorate process. From electrocatalysis to pilot plant investigations

© Kristoffer Hedenstedt, 2017

Cover illustration: Sketch of the sodium chlorate mild steel cathode during hydrogen evolution.

Department of Chemistry and Molecular Biology
University of Gothenburg
412 96 Gothenburg, Sweden

ISBN 978-91-629-0103-5 (print)
ISBN 978-91-629-0104-2 (PDF)
Available online at: http://hdl.handle.net/2077/52081

Printed by Ineko
Kållered, Sweden 2017

“Reality isn’t what it used to be.”

Dean Koontz, The Taking

Abstract

Sodium chlorate is an important industrial chemical produced through an electrochemical manufacturing process. The global production rate is 3.6 million tons annually and consumes approximately 20 TWh of electrical power. The majority of the produced sodium chlorate is used as raw material to make chlorine dioxide for the bleaching of kraft pulp. This thesis aims to provide a deeper understanding on the mild steel cathode and the role sodium dichromate has in the electrolyte in the chlorate process. Such understanding would allow reduction of the energy consumption, in particular, as well as the overall manufacturing footprint.

Two separate sodium chlorate plants have shown different performances in terms of current efficiency and corrosion of the mild steel cathodes. Surface characterisations and current efficiency measurements were performed on the two cathodes in order to evaluate the difference in performance between the samples. Two types of FeOOH were found on the individual cathodes: goethite (α-FeOOH) on the normally performing cathode and lepidocrocite (γ-FeOOH) on the poorly performing cathode. The two different FeOOH species were synthesised in pure form to elucidate if their electrocatalytic properties were the reason for their different performance. Both goethite and lepidocrocite showed lower activity for the reduction of water compared to polished mild steel but almost equally good towards hypochlorite reduction. The difference in performance of the pure phases can therefore not explain their differences in behaviour in large scale performance. However, *in situ* Raman spectroscopy revealed that the active species on the surface of the mild steel cathode was $Fe(OH)_2$ and the kinetics for the reduction of the surface from Fe(III) to Fe(II) was also found to be different between the two types of corrosion products. These findings are the reason for the observed differences in current efficiency.

Reduction of hypochlorite is the most important loss reaction in the chlorate process and Cr(VI) is added to the electrolyte to inhibit this reaction. A Cr(III) film formed at the cathode provide selectivity towards hydrogen evolution. The mechanism of hypochlorite reduction at Fe(III) and Cr(III) was studied by Density Functional Theory (DFT) calculations in order to understand the blocking effect of the Cr(III) film. The electro catalytic properties was shown to be very similar for Fe(III) and Cr(III) and cannot explain the blocking effect of Cr(III). However, the experimental results clearly demonstrated that the Cr(III) film was completely blocking of the hypochlorite reduction. It was concluded that it is the semiconductor properties of the materials that explain that the hypochlorite reduction at Cr(III) is inhibited while the reduction readily can proceed at iron (oxy)hydroxides.

A pilot plant was used to investigate the long term effects from continuous operation. Three process parameters were tested in the pilot plant to investigate the formation of different corrosion products on the cathode surface and their effect on the energy efficiency. These three were concentration of dichromate, sulphate and the temperature of the electrolyte. The pilot plant studies revealed possibilities to optimise the current efficiencies and corrosion of the cathodes with respect to the operating and shutdown conditions.

Finally recommendations are issued, as to how a sodium chlorate producer should relate to the results in order to minimize the losses in current efficiencies and cathodic corrosion.

Keywords: Sodium chlorate, corrosion, mild steel, goethite, lepidocrocite, green rust, hypochlorite reduction, hydrogen evolution, *in situ* electrochemical Raman spectroscopy

Sammanfattning

Natriumklorat är en viktig produkt som framställs i en elektrokemisk process. Årligen produceras cirka 3.6 miljoner ton globalt med en energiförbrukning på ungefär 20 TWh. Huvuddelen av det klorat som produceras utgör råmaterial vid tillverkningen av klordioxid vilken används för blekning av kemisk massa. Målet med den här avhandlingen är att få en djupare förståelse i hur stålkatoden fungerar samt att undersöka den roll natriumdikromat spelar i kloratelektrolyten. Denna kunskap kan användas för att både sänka energiförbrukningen samt minska miljöpåverkan av kloratproduktionen.

Elektroder från två kloratfabriker, som uppvisat skillnader i strömutbyten och korrosion, undersöktes som ett första steg. Ytanalyser och strömutbytesmätningar gjordes på elektroder från dessa fabriker för att förstå skillnaderna mellan dem. Två olika faser av FeOOH kunde identifieras på de två katoderna. På den normalt presterande fanns Götit (α-FeOOH) medan Lepidokrokit (γ-FeOOH) hittades på den katod som presterade sämre. De två olika typerna av FeOOH syntetiserades i sina rena former för att utvärdera om deras elektrokatalytiska egenskaper var anledningen till deras olika prestanda. Både Götit och Lepidokrokit visade lägre aktivitet mot reduktion av vatten jämfört med en nypolerad stålelektrod medan båda faserna visade sig även ha jämförbart lika låg aktivitet mot hypokloritreduktion. Således kan inte skillnaden mellan de rena faserna härledas till deras elektrokatalytiska egenskaper för vatten- respektive hypokloritreduktion. *In situ* Raman spektroskopi visade dock att den aktiva fasen på kloratkatoden, vid vattenreduktion, är $Fe(OH)_2$ och reduktionskinetiken från Fe(III) till Fe(II) visade sig variera stort mellan de två FeOOH faserna. Dessa resultat beskriver anledningen till de skillnader i strömutbyte som uppvisas under uppstart.

Hypokloritreduktionen är den största förlustreaktionen på katoden i kloratprocessen och natriumdikromat tillsätts till elektrolyten för att hindra den reaktionen. En film av trivalenta kromföreningar bildas på katoden som ger den dess selektivitet för vatten reduktion. DFT-beräkningar användes för att studera skillnader mellan Fe(III) och Cr(III) för att se om detta kunde beskriva kromfilmens blockerande effekt. De teoretiska beräkningarna visade inga skillnader hos de elektrokatalytiska egenskaperna mellan Fe(III) och Cr(III) som kunde förklara skillnaderna mellan ämnena. Experimentella studier bevisade dock tydligt att kromfilmen hindrar reduktion av hypoklorit. Detta tyder på att materialens inneboende halvledaregenskaper är orsaken till att den trevärda kromfilmen inhiberar reduktionen av hypoklorit medan vattenreduktion tillåts fortgå på järn (oxo)hydroxider.

En pilotanläggning användes för att studera långtidseffekter under kontinuerlig drift. Effekten från tre olika processparametrar testades i pilotanläggningen för att undersöka vilka korrosionsprodukter som bildas på katodytan samt hur de påverkar energieffektiviteten för processen. Dessa var processparametrar var koncentrationen av natriumdikromat, natriumsulfat och elektrolytens temperatur. Resultat från pilotanläggningen visade att det går att optimera strömutbyten och korrosion av stålkatoderna beroende på drifts- och stopparametrar.

Avslutningsvis så ges det handfasta rekommendationer för hur man som klorattillverkare skall styra processen för att minimera förluster i strömutbyten samt katodkorrosion.

Nyckelord: Natriumklorat, korrosion, låglegerat stål, götit, lepidokrokit, grönrost, hypoklorit reduktion, vätgasutveckling, i*n situ* elektrokemisk Raman spektroskopi

List of publications

This thesis is based on the work presented in the following four papers.

Paper I: **Study of Hypochlorite Reduction Related to the Sodium Chlorate Process**
K. Hedenstedt, A. Gomes, M. Busch and E. Ahlberg
Electrocatalysis, Vol 7, 4, pp 326-335 (2016)
DOI 10.1007/s12678-016-0310-5

Paper II: **Kinetic study of the hydrogen evolution reaction in slightly alkaline electrolyte on mild steel, goethite and lepidocrocite**
K. Hedenstedt, N. Simic, M. Wildlock and E. Ahlberg
Electroanalytical Chemistry, Vol 783, pp1-7 (2016)
DOI 10.1016/j.jelechem.2016.11.011

Paper III: **In-Situ Raman Spectroscopy of α- and γ-FeOOH during cathodic load**
K. Hedenstedt, J. Bäckström and E. Ahlberg
Submitted to Journal of Electrochemical Society

Paper IV: **Current Efficiencies of Individual Electrodes in the Sodium Chlorate Process: A Pilot Plant Study**
K. Hedenstedt, N. Simic, M. Wildlock and E. Ahlberg
Submitted to Journal of Applied Electrochemistry

Contribution list

Paper I:	Designed, performed and evaluated the electrochemical study and characterisation of α-FeOOH and γ-FeOOH. Contributed to writing of the paper.
Paper II:	Designed and performed all measurements. Evaluated the work with support from the co-authors. Lead author with support from the co-authors.
Paper III:	Designed and performed all measurements in collaboration with Joakim Bäckström. Evaluated the work with support from the co-authors. Contributed to writing of the paper.
Paper IV:	Designed and performed all measurements. Evaluated the work with support from the co-authors. Lead author with support from the co-authors.

Table of Contents

Abstract V

Sammanfattning VII

List of publications VIII

Contribution list IX

1. Introduction 1

1.1. Aim of the thesis 3

2. Sodium chlorate 5

2.1. Sodium chlorate formation 6

2.2. Energy consumption 7

2.3. Reactions related to energy losses 8

2.3.1. Anodic side reactions 8
2.3.2. Cathodic side reactions 9
2.3.3. Energy losses related to bulk reactions 10

2.4. Sodium dichromate 10

2.5. Current efficiency 12

3. Experimental techniques 15

3.1. Surface characterisation 15

3.1.1. X-Ray diffraction 16
3.1.2. Scanning electron microscopy 17
3.1.2.1. SEM imaging 17
3.1.2.2. Energy-dispersive X-ray analysis 18
3.1.3. Fourier transform infrared spectroscopy 18
3.1.4. Raman spectroscopy 19
3.1.4.1. *In situ* Raman spectroscopy 20

3.2. Electrochemical methods 21

3.2.1. Electrochemical cell 21
3.2.2. Rotating disc electrodes 22
3.2.3. Linear sweep voltammetry 23
3.2.3.1. Kinetic studies 24
3.2.4. Electrochemical impedance spectroscopy 25
3.2.4.1. Controlled-potential EIS 25

3.3. Electrode preparation 26

3.3.1. Rotating disc electrodes 26
3.3.1.1. Iron oxyhydroxide electrodes 26
3.3.1.2. Chromium (III) deposition 26
3.3.2. Flag electrodes 27
3.3.3. Carbon paste electrodes 27
3.3.4. Pilot plant cell electrodes 27

3.4. Process-like conditions / pilot cell 27
  3.4.1. Electrolyte 29
  3.4.2. Method 29

4. Results and discussion 31

4.1. Study of sodium chlorate process cathodes 31
  4.1.1. Influences of operating conditions on the cathode corrosion 33
    4.1.1.1. Operating conditions for the extracted plant electrodes 33
    4.1.1.2. Laboratory-scale corrosion studies 33
  4.1.2. Power consumption study on process cathodes 34

4.2. Kinetic investigations on α- and γ-FeOOH 35
  4.2.1. Synthesis and stability of α- and γ-FeOOH phases on electrodes 35
  4.2.2. Kinetics of hypochlorite reduction 38
  4.2.3. Hydrogen evolution kinetics 40
  4.2.4. Concluding remarks regarding kinetic studies 41

4.3. *In situ* Raman studies of the reduction of α- and γ-FeOOH 42

4.4. Studies on the effects of dichromate in the chlorate process 45
  4.4.1. Sodium dichromate and cathodic current efficiency 45
  4.4.2. Sodium dichromate and oxygen evolution 46
  4.4.3. Stability of the chromium (III) film 47

4.5. Temperature effects on the chlorate process 48

4.6. Sulphate effects on the chlorate process 49

4.7. Corrosion at the cathode 49

5. Conclusions and recommendations 53

5.1. Conclusions 53

5.2. Recommendations for future work 54

5.3. Recommendation for sodium chlorate producers 55

Acknowledgements 57

Bibliography 59

1. Introduction

Why do the steel cathodes in the sodium chlorate cell work even though they severely corrode? What processes do these cathodes undergo during operation and while the process is shut down? Why do these cathodes perform differently in different plants even though they are composed of the same material? These rather large questions require complex answers. In this thesis, I will shed light on this complicated matter, and after reading it, you will be a bit older, a bit wiser, and if you run a sodium chlorate plant, you will be able to be a bit more sustainable.

Sodium chlorate ($NaClO_3$) is the salt of chlorine in its pentavalent (+V) state. Annually, approximately 3.6 million tons of sodium chlorate is produced worldwide, and the majority, more than 90 %, is used in the pulp industry [1-3]. Sodium chlorate is a powerful oxidiser and is therefore commonly used in pyrotechnical applications. As a potassium salt, chlorate is used in safety matches. Other uses for chlorates are as chemical oxygen generators in aircraft and submarines and for the extraction of uranium [1].

In the pulp industry, sodium chlorate is used for producing chlorine dioxide (ClO_2) [1]. Chlorine dioxide is the main active bleaching agent in the elemental chlorine-free (ECF) bleaching sequence for kraft pulp. The major turning point for the use of chlorine dioxide occurred in the late 1980s and early 1990s with the emerging concerns about the environmental impacts of using elemental chlorine [4]. Using chlorine dioxide has become the dominant bleaching method, and most new installations adopt this technique. In 2010, ECF bleaching accounted for more than 90 % of the market [5]. The ECF technique is environmentally friendly and has established its role as the best available technique [6]. No other alternative bleaching agents provide the same brightness while retaining the strength of the pulp, good economy and a very low environmental impact. Chlorine dioxide is thermodynamically unstable and contains an un-paired electron, which makes it highly reactive. Therefore, the storage of chlorine dioxide is limited to dilute water solutions in holdup tanks, and its transportation is not feasible for practical and safety reasons. Chlorine dioxide must consequently be produced in close vicinity to the application at the pulp mills, called “on-site production”. Sodium chlorate is, despite its oxidising property, safer to handle than chlorine dioxide and can be transported either as the dry salt or in aqueous solution. At the pulp mill, the chlorate is reduced to chlorine dioxide in a chlorine dioxide reactor using proper reducing agents, such as hydrogen peroxide or methanol, under acidic conditions, and the produced chlorine dioxide can be immediately used in the bleaching application [4, 6, 7].

Today, sodium chlorate is produced through an electrosynthesis route that was developed in the late 19th century [8]. The process is highly energy intensive, and although progress has been made over the years in reducing the power consumption, there is still more energy to be saved. The heart of the sodium chlorate process is the electrochemical cell, which also accounts for largest energy consumption. These cells are the host for two main electrochemical reactions, which are chloride oxidation to chlorine on the anode and water reduction to hydrogen and hydroxide ions on the cathode. The energy consumption in an electrochemical process is proportional to the cell voltage. In Figure 1.1, the potential distribution over the cell gap is shown to illustrate where the losses occur. The total potential in Figure 1.1 is based on a fairly normal cell voltage of 3.0 V.

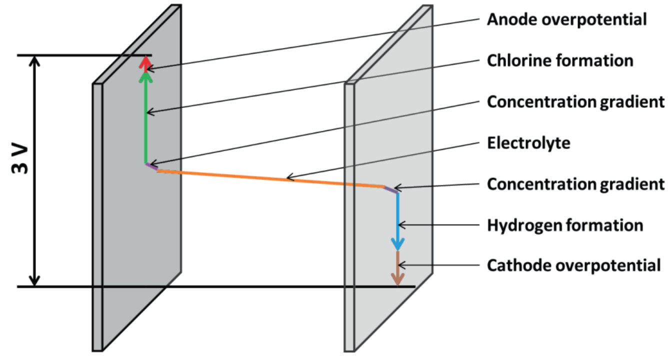

Figure 1.1 Schematic view of the distribution of potentials in a sodium chlorate cell based on a representative cell voltage of 3.0 V and an inter-electrode distance of 3 mm.

The thermoneutral voltage is the theoretical value of the potential required for the reactions, and it is determined from the formation enthalpy and entropy of the species. Its value cannot be lowered unless the reactions involved are exchanged. The thermoneutral voltage for chlorine evolution is 1.36 V vs. the normal hydrogen electrode (NHE), and its contribution to the total cell voltage is shown in Figure 1.1. The corresponding thermoneutral voltage for hydrogen evolution at an estimated surface pH of 11 is approximately -0.65 V vs. NHE, as shown in Figure 1.1 [9]. The surface pH at the cathode is alkaline since hydroxide ions are formed in the hydrogen evolution reaction (HER). The HER is pH dependent, but it is not possible to lower this formation voltage by decreasing the pH without affecting the formation of chlorate in the bulk. Lowering the pH will also increase the desorption of chlorine, causing a higher demand and costs for acids and caustics. To force an electrochemical reaction to proceed, an additional voltage needs to be applied on top of the thermoneutral voltage. This additional voltage is called overvoltage or overpotential. The overpotentials of chlorine and the HER are also illustrated in Figure 1.1. The anodic overpotential for chlorine evolution is very small due to the efficient electrocatalyst available for commercial dimensionally stable anode (DSA) electrodes [10]. However, at the cathode, the overpotential for hydrogen evolution is quite high. In the chlorate process, the cathode is normally composed of mild steel with an overpotential of approximately 390 mV (13 % of the total cell voltage).

The second largest loss contributing to the cell voltage is the electrolyte resistance between the two electrodes, which is approximately 260 mV (almost 9 %). However, the distance between the electrodes is only a few mm. This loss is also called the iR drop, and it depends on the conductivity of the electrolyte, the distance between the electrode blades and gas bubbles in the electrode gap. These parameters are difficult to influence. There is little to gain by improving the conductivity of the electrolyte. The conductivity can be improved by diluting the electrolyte, but this will increase the energy consumption for crystallisation. The distance between the electrodes is also a compromise between an improvement in energy consumption and safety since a short circuit between two electrode blades will burn a hole at the contact surface and may cause an explosion from ignition of the hydrogen gas. The remaining part of the losses is related to the stagnant hydrodynamic layer and concentration gradients in close vicinity to both electrodes (100 mV, 3.3 % on the anode and 250 mV, 8.3 % on the cathode) [9]. To be able to reduce these losses, the dynamics of the electrolyte flow within the cells needs to be changed, which can only be achieved if the cells are redesigned.

Consequently, focusing on lowering the overpotential of the cathode would lead to the greatest impact on lowering the energy consumption in the sodium chlorate process. As previously mentioned, the cathodes used are mild steel, which is a low alloy steel with small amounts of carbon. Thus far, this material provides the lowest cost and energy consumption in the process with respect to endurance, price and current efficiency. Although the mild steel cathode is the state of the art, it has one major drawback. During shutdown, it severely corrodes, and it has been proven to provide, under certain circumstances, a low current efficiency [11]. Understanding the properties and behaviour of the cathode under process conditions, i.e. which corrosion products are formed and how they behave, will help to optimise the cathode and the operating conditions for the process.

1.1. Aim of the thesis

The overall goal of this thesis is to obtain insights into how to substantially lower the energy consumption in the sodium chlorate process. The research strategy that is adopted in this work is a top down and back up approach, starting from industrial conditions, going down to a molecular understanding and ending in pilot studies and recommendations for full-scale plants. Significantly aged electrodes were collected from two different sodium chlorate plants with different performances. These two plants, which were constructed based on the same technology, showed different current efficiencies and corrosion behaviours. The corrosion products at these cathodes were analysed, and the electrochemical performance of the electrodes was verified in laboratory tests. Pure reference compounds of the substances found at the electrode surfaces were synthesised and characterised with respect to electrochemical properties, such as the kinetics of hypochlorite reduction and hydrogen evolution. *In situ* Raman studies were performed to verify the active species on the cathode surface during operation. Finally, the influence of different process parameters on performance and corrosion was investigated under simulated full-scale conditions in a long-term test in a pilot plant. The findings made in this thesis work will be used in the development of new recommendations for full-scale operation.

2. Sodium chlorate

The industrial-scale production of sodium chlorate dates back to the end of the 19th century. It is produced through an electrosynthesis route that is still based on the same concept, although it has been developed to decrease the power consumption and significantly improve raw material utilisation. Most producers of chlorate currently utilise a closed-loop system where sodium chloride, water and electric energy are added to the process while sodium chlorate and hydrogen gas are withdrawn [1, 8, 9].

The production of chlorate follows three main steps: brine purification, electrolysis and crystallisation. The electrolysis system with the electrolytic cells is considered to be the heart of the process. All main flows in the process can be viewed in the schematic presented in Figure 2.1. The electrolysers are situated together with the reactor tank in the main circulation loop. The electrochemical reactions and most of the wanted bulk reactions occur in the electrolyser. The reactor tank is used to complete the wanted conversion to chlorate. The main loop circulating over the cells and reactor tanks is almost a completely closed system. Before the sodium chloride and water are added, they need to pass through the brine purification system. This step is of great importance to avoid the build-up of high concentrations of impurities in the main loop. Because the main loop is almost completely closed, even the smallest amounts of an impurity will be accumulated at process-disturbing concentrations. These impurities can affect the current efficiencies and lead to unwanted reactions yielding increased oxygen evolution in the cell and hence causing a safety issue. Some impurities may also crystallise with the product and give rise to problems in the chlorine dioxide generators. After the cells, the gas and electrolyte are separated. The gas is purified in a scrubber system, where desorbed chlorine species are removed. The purified hydrogen is mostly used downstream as a raw material or for combustion. A small side stream of the electrolyte is removed from the main loop for crystallisation of the chlorates. The chlorate crystals from the crystalliser are washed and then either dried and packed as crystals or re-dissolved and delivered as an aqueous solution. The chlorate-depleted brine in the crystalliser is returned to the main loop through the salt dissolver in the brine purification system. The typical electrolyte consists of approximately 100 to 150 gdm^{-3} sodium chloride, 450 to 630 gdm^{-3} sodium chlorate, and 2 to 7 gdm^{-3} sodium dichromate at pH 6 to 7 and the operating temperature is between 70 to 90 °C [12, 13].

The addition of hydrochloric acid and a caustic is needed to control the pH in the process. Some chlorine desorbs from the cells and tanks, causing a shortage of chlorides. This situation is mitigated by alkaline scrubbers. To protect the crystallisers from corrosion, the electrolyte is alkalised. The added alkali must overall be balanced by the addition of hydrochloric acid [2]. Sodium dichromate is added to the electrolyte to suppress unwanted reactions on the cathode. This will be discussed later but is the reason for why the manufacturing facilities should be built as closed-loop plants. The release of any hexavalent chromium (Cr(VI)) to the environment must be avoided; hence, the use of Cr(VI) must be carefully monitored [14-16].

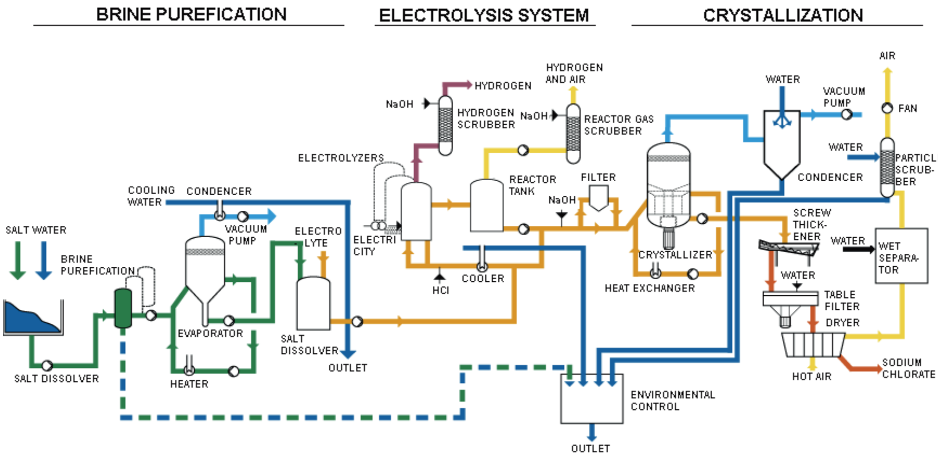
BRINE PUREFICATION
ELECTROLYSIS SYSTEM
CRYSTALLIZATION
AIR
HYDROGEN AND AIR
WATER
HYDROGEN
VACUUM PUMP
FAN
NaOH
HYDROGEN SCRUBBER
NaOH
REACTOR GAS SCRUBBER
WATER
PARTICLE SCRUB-BER
ELECTROLYZERS
CONDENCER
REACTOR TANK
FILTER
COOLING WATER
CONDENSER
NaOH
SCREW THICK-ENER
SALT WATER
VACUUM PUMP
ELECTRO LYTE
ELECTRI CITY
WATER
WET SEPARA-TOR
BRINE PUREFICATION
CRYSTALLIZER
HCl
COOLER
WATER
HEAT EXCHANGER
TABLE FILTER
EVAPORATOR
SALT DISSOLVER
DRYER
OUTLET
SODIUM CHLORATE
SALT DISSOLVER
HEATER
HOT AIR
ENVIRONMENTAL CONTROL
OUTLET

Figure 2.1 Schematic flow diagram of the sodium chlorate process (Courtesy of AkzoNobel Pulp and Performance Chemicals (PPC) AB, Sweden).

The schematic in Figure 2.1 is an example of how a plant may be set up. Different brine purification steps or crystallisers may be used. Several different cell designs are also used in production and are described in the literature [9, 13, 17, 18].

2.1. Sodium chlorate formation

The overall reaction that occurs in the process is the neutral pH formation of $NaClO_3$ and hydrogen from sodium chloride and water (1).

$$NaCl + 3H_2O \rightarrow NaClO_3 + 3H_2 \qquad (1)$$

This reaction requires considerable energy, and it will be discussed in Section 2.2. Chlorate was originally produced chemically by leading chlorine through a caustic and pot ash, but when high power sources became available, the electrosynthesis route became the preferred process [18].

The chlorate formation simplified in the overall reaction (1) proceeds through several reaction steps. First, there are two main electrochemical, heterogeneous steps, (2) and (3), which are followed by homogenous, pure chemical reactions occurring in the bulk. The electrochemical steps are chloride oxidation to chlorine (2) on the anode and water reduction to hydrogen and hydroxide (3) occurring on the cathode.

Anodic chloride oxidation

$$2Cl^- \rightarrow Cl_2 + 2e^- \qquad (2)$$

Cathodic water reduction

$$2H_2O + 2e^- \rightarrow H_2 + 2OH^- \qquad (3)$$

The hydroxide is consumed in the intermediate reaction steps, maintaining pH neutrality in the overall reaction (1).

Chlorine is formed at the anode in the gaseous phase, but it is instantaneously dissolved in the electrolyte. The dissolved chlorine is further hydrolysed (4) to form hypochlorous acid.

$$Cl_2 + 2H_2O \rightarrow Cl^- + HClO + H_3O^+ \tag{4}$$

Reaction (4) occurs in close vicinity to the anode, leading to a lower pH than in the bulk electrolyte. In the bulk, the hypochlorous acid is partially deprotonated due to its acid-base equilibrium (5). Chlorate is subsequently formed by the disproportionation reaction (6) between two hypochlorous acid molecules and one hypochlorite ion.

$$ClOH + H_2O \rightarrow ClO^- + H_3O^+ \tag{5}$$

$$2ClOH + ClO^- \rightarrow ClO_3^- + 2Cl^- + 2H_3O^+ \tag{6}$$

The chlorate formation reaction has its highest rate at the pH where the ratio between hypochlorous acid and the hypochlorite ion is 2:1. However, there are more parameters that influence the choice of optimum pH for the process, such as the desorption of chlorine due to reaction (4) and higher decomposition of hypochlorous acid (further discussed in 2.3.3.). Therefore, the cells are generally operated at a slightly more alkaline pH to increase the overall efficiency [9, 19].

2.2. Energy consumption

As previously mentioned, the chlorate process is a highly energy-demanding process. To calculate the energy needed in the electrochemical step in the process, one has to start with the work function (7).

$$P = \frac{QV}{t} \tag{7}$$

where P is the work done per unit time, Q is the total amount of electric charge in coulombs, V is the electric potential or more commonly the cell voltage, and t is the time in seconds. From Faraday's law (8), one obtains the relationship between how much charge is required to produce a specific amount of chlorate.

$$Q = \frac{mnF}{M} \tag{8}$$

Faraday's constant, F, is the link between coulombs and moles, m is the mass in grams, n is the stoichiometric number of electrons used per chlorate ion, and M is the molar mass. To facilitate the main reaction (1) electrochemically, 6 moles of electrons are used for each mole of sodium chlorate produced. The energy needed for the electrochemical formation of sodium chlorate given in kWh per ton is given in equation (9) using 10^6 grams per ton and 3600 seconds per hour.

$$P = \frac{mnFV}{Mt} = \frac{10^6 \times 6 \times 96485}{106.44 \times 3600 \times \varepsilon} \times V = \frac{1511 \times V}{\varepsilon}\left[\frac{kWh}{ton}\right] \tag{9}$$

To relate the electric potential to the chlorate cell, V, to the power consumption, it is also necessary to take the side reactions occurring in the cell into account; therefore, the term for current efficiency, ε, is introduced. The power consumption in the cell is consequently dependent on the cell voltage and the current efficiency.

There is a theoretical minimum for the energy consumption, which can be calculated from (9). This minimum can be derived if one assumes that the current efficiency is 100 %, but the cell voltage still needs to be entered in the equation. To determine the lowest possible cell voltage required to produce sodium chlorate, one needs to calculate the thermoneutral voltage, i.e. $V = E_C^0$. The thermoneutral voltage for the formation of a species is given by Gibb's free energy (ΔG^0) divided by the number of electrons and Faraday's constant (10). Alternatively, the use of formation enthalpy ($\Delta_r H^0$) and entropy ($\Delta_r S^0$) can be employed.

$$E_C^0 = -\frac{\Delta_r G^0}{nF} = -\frac{\left(\Delta_r H^0 - T\Delta_r S^0\right)}{nF} \tag{10}$$

The thermoneutral voltage for the formation of sodium chlorate is 1.618 V, and using this value in (9), the absolute minimum energy necessary for electrolytic formation will be 2.445 MWh ton^{-1}. Today, commercial sodium chlorate cells are operating at voltages ranging from 2.85 to 3.30 volts and have current efficiencies of approximately 92 to 95 %. This provides a range of 4.5 to 5.4 MWh ton^{-1}; hence, the possibility to save energy is substantial. However, the lowest theoretical energy needed would be 3.8 MWh ton^{-1} since several losses are difficult to overcome, such as electrolyte resistance in the cell gap and alkaline hydrogen evolution [3, 9].

2.3. Reactions related to energy losses

The initial chlorate process was extremely inefficient with a current efficiency as low as 37 % [18], whereas the modern chlorate process has been optimised over the years to achieve high current efficiencies of 92 to 95 % [3, 9]. However, an improved current efficiency of even a few percent will have considerable economic and environmental impacts due to the high energy consumption and the large volume produced. There are several reasons for current efficiency losses in the process. Some of the losses are due to side reactions occurring on the electrodes; thus, the electrocatalytic properties of the electrodes are critical. Other loss reactions occur in the bulk electrolyte, thereby placing special demands on process control. There are also losses from chlorine and hypochlorous acid that desorb from the liquid phase and follow the cell gas [20].

2.3.1. Anodic side reactions

When Henry Beer developed the DSA, which primarily consists of ruthenium dioxide-coated titanium, a huge leap in reducing energy consumption was achieved on the anodic side [10]. The selectivity of the DSA is by far better than that of the previously used graphite electrodes, and the DSA also has a low overpotential towards chlorine evolution. The oxygen concentrations in the chlorate cell gas today are approximately 2 %. Calculating the total losses due to the anode with respect to oxygen formation and overpotential places it on the order of 0.4 MWh ton^{-1}. This value is slightly uncertain due to oxygen formation from the bulk, thus making it difficult to fully validate [21]; see Sections 2.3.3 and 2.5.

The main reaction on the anodes is chloride oxidation into chlorine gas (2). However, there are some competitive reactions occurring on the anodes leading to a reduced current utilisation. The anodic side reactions are mainly oxygen-forming reactions, such as water or hypochlorite oxidation. These reactions are of major concern since an explosive mixture is obtained at 4 % oxygen in the hydrogen cell gas. The suggested oxygen-forming reactions that occur are as follows [20, 22]:

$$12ClO^- + 6H_2O \rightarrow 4ClO_3^- + 12H^+ + 6Cl^- + 3O_2 + 12e^- \tag{11}$$

$$ClOH + H_2O \rightarrow 3H^+ + Cl^- + O_2 + 2e^- \tag{12}$$

$$2H_2O \rightarrow O_2 + 4H^+ + 4e^- \tag{13}$$

There have been discussions regarding which reaction or reactions dominate the oxygen formation, but difficulties in separating the different contributions have also been noted [17, 20, 22].

Perchlorate formation (14) is a reaction that is feasible from a thermodynamics perspective and is constantly ongoing in the chlorate process. However, this reaction is kinetically hindered and proceeds at a very low rate. This reaction is dependent on the selectivity of the anode and is generally kept under control. As the anode ages, the selectivity for chloride oxidation will decrease and both the oxygen concentration in the cell gas and the perchlorate concentration in the electrolyte will increase [17].

$$ClO_3^- + H_2O \rightarrow ClO_4^- + 2H^+ + 2e^- \tag{14}$$

2.3.2. Cathodic side reactions

Mild steel is the most commonly used material for cathodes in modern chlorate plants, which is why this thesis work focuses on this material. Steel cathodes have moderately high overpotentials against the HER, 250 to 400 mV [3], and they are relatively inexpensive. However, due to the oxidising environment, these cathodes severely corrode during shutdowns. This property is beneficial because a very large surface area is created, but it is detrimental for the working life of the electrodes.

Some plants are still using titanium as a cathode material even though it has an approximately 300 mV higher overpotential compared to mild steel. In addition, the titanium cathodes need to be exchanged after approximately two years due to titanium hydride formation. Several other cathode materials have been tested with the aim of reducing the overpotential, such as ruthenium-coated titanium [23], ceramics [24] and other substrates [25, 26]; however, no better alternatives have been commercialised. The mild steel electrode is not selective towards hydrogen evolution; on the contrary, it has been proven to be very active for hypochlorite reduction, which is why sodium chromate is added to the electrolyte to eliminate this reaction. Further reading about chromium can be found in Section 2.4 [8, 14-16, 19].

On the cathode, the desired process is the HER (3). There are two parasitic reactions that occur on the cathodes, which are responsible for the majority of the current efficiency losses. These reactions are hypochlorite reduction (15) and chlorate reduction (16) [15, 16].

$$ClO^- + H_2O + 2e^- \rightarrow Cl^- + 2OH^- \quad (15)$$

$$ClO_3^- + 3H_2O + 6e^- \rightarrow Cl^- + 6OH^- \quad (16)$$

2.3.3. Energy losses related to bulk reactions

In the bulk electrolyte, chlorine gas hydrolyses to hypochlorous acid, reaction (4), which deprotonates according to the acid-base equilibrium (5). The hypochlorous acid and hypochlorite disproportionate according to reaction (6), forming chlorate. However, there are two important reactions leading to energy losses in the bulk. The first is the desorption of chlorine into the cell gas (17).

$$Cl_2(aq) \rightarrow Cl_2(g) \quad (17)$$

The chlorine desorption results in not only losses in current efficiency but also losses in the subsequent reactions (4), (5) and (6). This will lead to proton depletion, and the balance between protons formed from chlorine hydrolysis and hydroxide produced at the cathode from hydrogen evolution (3) will be skewed. This loss of chlorine to the cell gas turns the electrolyte alkaline, and the pH in the cell increases. The majority of this loss can be reduced using caustic scrubbers, which trap the chlorine and bring hypochlorite and chloride back to the process, thereby mitigating the current efficiency loss [2]. However, both pH control and the need for caustic scrubbers lead to increased production costs.

The decomposition of hypochlorous acid is the second reaction leading to energy losses in the electrolyte (18). Another issue of this reaction is that it produces oxygen, which leads to increased safety concerns [20].

$$2ClOH \rightarrow O_2 + 2Cl^- + 2H^+ \quad (18)$$

To suppress this reaction, the pH in the cell should be kept high enough to drive reaction (5) slightly to the right. This will allow the formation of chlorate to occur but the decomposition of hypochlorous acid to be minimised.

2.4. Sodium dichromate

One of the first records found that mentions the use of sodium dichromate in the chlorate process was the Swedish patent filed by Johan Landin in 1892 [14]. This patent was shortly followed by a couple of papers [8, 19] reporting an increase in current efficiency through the addition of sodium chromate. Over the years, several studies have been conducted with the aim of understanding the role and mechanisms that dichromate have in the chlorate process [11, 15, 16, 19, 22, 27-33]. One important function of the dichromate added to the chlorate process is that it contributes buffering effects in the desired pH ranges. The dichromate is in equilibrium with chromic acid in the electrolyte (19).

$$Cr_2O_7^- + H_2O \leftrightarrow 2HCrO_4^- \quad (19)$$

The following chemical reactions of chromic acid are relevant for buffering the electrolyte:

$$CrO_4^{2-} + H^+ \leftrightarrow HCrO_4^- \quad (20)$$

$$HCrO_4^- + H^+ \leftrightarrow H_2CrO_4 \quad (21)$$

The pK_a for (20) is reported to be in the range of 5.8 to 6.5, and for (21), it is approximately 1 [17, 34-36]. This pK_a provides buffering effects in the optimal regions, both in the bulk electrolyte where the chlorate formation rate is at its highest and on the anode. The buffering effect around pH 1 on the anode keeps the pH from becoming too low [37]. Low pH increases the selectivity for chlorine evolution, but chlorate will be reduced to chlorine dioxide by chlorides when the pH is too low [38, 39]. It has been shown that the presence of chromate in the electrolyte promotes the chlorate formation reaction, lowers the hypochlorite levels in the electrolyte and diminishes the hypochlorite decomposition and oxygen levels [28].

The most important role that sodium dichromate has in the chlorate process is providing selectivity to the steel cathode. It has been shown that dichromate is reduced *in situ* from a hexavalent state to a trivalent chromium film covering the cathode. This *in situ* formed film effectively hinders the reduction of hypochlorite and chlorate while still allowing the hydrogen evolution to proceed [15, 16]. The true structure of the film has not yet been fully proven, but authors discuss whether it is Cr_2O_3, $Cr(OH)_3$ or a hydrous mixture of the type $CrOOH(xH_2O)$ film [8, 15, 30-32]. The thickness of the film was studied by Lindbergh et al. on platinum [30] and on gold [31]. Ahlberg Tidblad et al. later conducted a study on the thickness of the deposited layer [32]. The results showed that the thickness varies with the substrate, is concentration dependent, and at 15 mM $Na_2Cr_2O_7$, it takes more than 9000 seconds to fully build up the thickness of the trivalent chromium film. How the thickness of the film behaves on mild steel cathodes is still unknown. It has also been suggested that the film is oxidised back to the hexavalent state by the hypochlorite ions in the electrolyte during shutdowns [11, 40]. This means that the film is destroyed during shutdowns and needs to be rebuilt on the next start-up. In addition, chromium acts as a strong corrosion inhibitor for the steel cathodes, substantially prolonging their lifetime [9, 22, 28].

Without chromium, the process would suffer from severe energy losses and high oxygen concentrations in the cell gas [18]. However, the use of hexavalent chromium is disputed because of its impact on health and the environment. Hexavalent chromium is toxic, carcinogenic, reprotoxic and mutagenic and should therefore be handled with the utmost care. The European Union has decided, due to the REACH legislation, that all use of hexavalent chromium shall be banned in September 2017 [41] unless an *authorisation for use* is given. Due to its hazardous properties, substantial efforts have been made to eliminate chromium in the chlorate process; thus far, however, it has not been successful, although significantly decreased levels of chromium have been proposed [42-46]. One commercialised alternative technique for reducing the risk of exposure to hexavalent chromium is to add the less harmful trivalent chromium in place of hexavalent chromium in the electrolyte since these will be oxidised to the hexavalent state inside the process [40]. In this way, the transportation of concentrated hexavalent chromium to the world's chlorate plants is eliminated, as well as the handling when adding the chromium to the plant, thereby providing significant occupational health benefits. However, this does not prevent the risk of possible exposure to hexavalent chromium when handling the electrolyte, electrolyte sludge and filter sludge. Today, these risks are mitigated using personal protective equipment and/or exhaust ventilation.

2.5. Current efficiency

As previously mentioned, the current efficiency factor in the chlorate process is of major concern when discussing power consumption. With a DC power consumption of 4250 to 5500 kWh ton^{-1} and current efficiency of 92 to 95 % [1, 9, 13], it is obvious that for the annual production of 3.6 million tons, even a slight increase in energy efficiency will result in substantial energy savings. The energy efficiency can be calculated in a number of ways, all with advantages and limitations, which will be discussed here. For full-scale plants, the overall efficiency is the most important issue, and it is fairly easy to measure the amount of chlorate produced and relate it to the energy consumed. The calculation for most unit operations in the plant is likewise straightforward. However, calculating the electrolytic current efficiency in the electrolysis cell is slightly more complicated. A true current efficiency analysis would be to perform the electrolysis for a specific amount of time and analyse the chlorate formed. However, this would require continuous sampling of the electrolyte followed by analysis with high accuracy. This would be difficult to use following the relatively fast processes during start-up and the lack of a method for analysing small differences in chlorate with high accuracy. Another approach is to analyse the cell gases, which are simple to quantify by measuring gas flow and concentration. As shown in reactions (2-3) and (11-13), the cell gas includes hydrogen from the cathode and oxygen from the anode. Using analytical techniques requires that the desorbed chlorine and water are removed. One concern with this method is that the oxygen measured is not purely electrochemically produced since the decomposition of hypochlorous acid in the electrolyte will generate oxygen. A second concern is that perchlorate formation will not be observed at all with this analysis. An equation for calculating the current efficiency was proposed by Jaksić et al. [47]:

$$\eta_{ClO_3} = \frac{100 - 3\%O_2 - 2\%Cl_2}{100 - \%O_2 - \%Cl_2} \qquad (22)$$

A revised version without measuring the chlorine was proposed by Tilak and Chen [21]:

$$\eta_{ClO_3} = \frac{\%H_2 - 2\%O_2}{\%H_2} \qquad (23)$$

A slightly different approach has been used in this work. It is based on Tilak and Chen’s equation, but the anodic and cathodic contributions are separated. Since the only gas emerging from the cathode is hydrogen, the cathodic current efficiency (CCE) can be calculated from the amount of hydrogen produced in ratio with the theoretical production.

$$CCE = \frac{\tilde{n}H_{2meas.}}{\tilde{n}H_{2theo..}} = \frac{\tilde{n}H_{2meas.}2F}{I} \qquad (24)$$

Only the oxygen formation is needed when considering the anodic current efficiency (ACE). In this calculation, the current efficiency is back calculated from 100 % and subtracting the part of the current used for producing oxygen.

$$ACE = 1 - 2\frac{\tilde{n}_{O_2 meas.}}{\tilde{n}_{O_2 theo.}} = 1 - 4\frac{\tilde{n}_{O_2 meas.} F}{I} \tag{25}$$

where $\tilde{n}$ in (24) and (25) is a term for the molar flow of the species per second. I is the current in amperes, and F is Faraday's constant. The constant 2 in (24) is because hydrogen requires 2 electrons to be formed, and in (25), the constant becomes 4 since oxygen needs 4 electrons. Moreover, in this case, oxygen from both water reduction and the decomposition of hypochlorous acid or hypochlorite are included.

3. Experimental techniques

As previously mentioned, this study used a top down and back up approach, starting from actual industrial electrodes collected from two different sodium chlorate plants, proceeding with fundamental electrochemical studies of the kinetics of the corrosion products found and ending in pilot-scale evaluation. Several different techniques have therefore been used in this work, which can be divided into three different groups: surface characterisation, electrochemical investigation and process-like operation.

The surfaces of the industrial electrodes were analysed to determine the types of species that were present on the electrodes. Pure reference compounds of the predominant substances found were synthesised and electrochemically characterised towards the reduction of hypochlorite and water. *In situ* Raman measurements were performed on the specific species to determine changes during polarisation and hydrogen evolution. To complete the circle, a pilot plant was constructed, and experiments were performed under simulated full-scale conditions to capture long-term effects and to consolidate the fundamental findings with the findings from the full-scale electrodes.

3.1. Surface characterisation

Surface characterisation is a key aspect in this work since the influence of different corrosion products on electrochemical kinetics or current efficiencies is still unknown and is within the scope of this work. Surface characterisation was performed using X-ray diffraction (XRD) to determine crystalline structures, scanning electron microscopy (SEM) to obtain a visual image of the surface and measure the crystal sizes, and energy-dispersive X-ray (EDX) spectroscopy to examine the elemental composition and distribution on the surfaces. Fourier transform infrared (FTIR) spectroscopy was used as a complement to XRD for amorphous phases, and Raman spectroscopy was used for *in situ* analyses on the electrode surfaces.

3.1.1. X-Ray diffraction

XRD is a technique used for determining crystal structures, and it provides an exact speciation of crystalline samples. A crystal structure that is radiated with X-rays causes the X-rays to diffract in many specific directions. Measuring the angles and intensities of the diffracted beams provides information that can be used to determine the positions of the atoms in the crystal structure. This technique originates from the diffraction of X-ray light on the different crystal planes of a substance. W. L. Bragg determined the relationship between how the wavelength of X-rays and the distance between planes correlates to the angle of diffraction, which is known as Bragg's law (22) [48].

$$n\lambda = 2d\ \sin\theta \qquad (22)$$

In Bragg's law, *n* is an integer, λ is the wavelength of the X-ray, d is the interatomic distance between the lattice planes, and θ is the angle at which diffraction occurs.

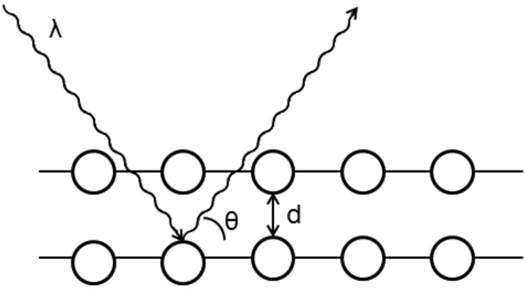

Figure 3.1 Simplified view of the principle behind the Bragg equation.

Bragg's equation is not sufficient for describing everything in an XRD analysis, but all aspects of such analyses are derived from this equation. The distances between different lattice planes depend on the crystal structure and sizes of the atoms. Depending on the crystal structure, only certain lattices may exist; consequently, all crystalline materials have their own unique diffraction pattern. This makes XRD a direct analysis method for the speciation of crystalline materials.

To perform an analysis that is as accurate as possible, all lattice planes should be visible to the X-rays such that they can reflect. This is achieved if the sample is a powder and the crystals are randomly orientated such that reflections occur at all planes, although solids may also be used. Occasionally, the sample orients itself into an organised structure that shows high reflections from a certain orientation. This is called preferential orientation and may occur if the sample is a solid or pressed too much to obtain a flat surface. In the diffractogram, preferential orientation appears as unnaturally high or lost peaks. This phenomenon is common and could make the analysis of the sample difficult or even impossible from only XRD measurements. Additional analysis is then needed to verify which substances are present.

In this work, a Siemens D5000 diffractometer was used. The radiation source was $Cu_{k\alpha}$ 1.5418 Å with a grazing angle of 5°. A monochromator was used before the detector to eliminate fluorescence from iron.

3.1.2. Scanning electron microscopy

SEM is an imaging technique that is more powerful than conventional optical light microscopy. SEM uses an electron beam that scans the sample surface rather than visible light. The electron beam has a considerably shorter wavelength than visible light and generates higher resolution images. In addition to imaging, SEM can provide atomic contrasts, and elements hit by electrons will also generate characteristic X-rays that can be analysed with EDX spectroscopy [49, 50].

3.1.2.1. SEM imaging

SEM images are generated from a highly focused electron beam that scans the surface. The electrons that hit the surface can either inelastically scatter back (secondary electrons), elastically scatter (backscattered electrons) or excite the core electrons, which emit X-rays when they relax. The electron beam is generated from either a coarse and low power thermionic gun with a filament of tungsten or LaB_6 or the thinner and stronger field emission gun (FEG). Before reaching the sample, the beam passes through a series of magnetic lenses and a scanning coil to focus and control the position of the beam, as shown in Figure 3.2.

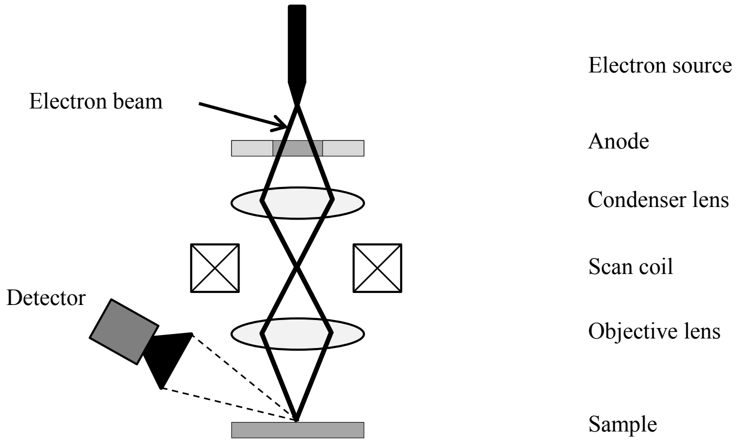

Figure 3.2 Electron paths in a scanning electron microscope.

For high-resolution images, using the secondary electrons is preferred due to their low interaction volume. The inelastic scattering comes from the outermost layer and emerges from loosely bound electrons that are knocked out by the primary beam. Images from the secondary electrons provide good topographic contrast and have a large depth of focus. Although the primary beam penetrates deeper into the sample and the electrons elastically scatter back, they give rise to a different type of signal. The amount of backscattered electrons depends on the atomic number, Z. The higher the Z is, the more they backscatter. This property provides the possibility of obtaining Z contrast images in which the heavier elements are brighter.

A Leo Ultra 55 SEM equipped with a FEG was used in this work. For imaging purposes, an accelerating voltage of approximately 3 kV was used.

3.1.2.2. Energy-dispersive X-ray analysis

As a complement to SEM images, EDX analysis is often used. EDX is a spectroscopic method in which the elements and atomic percent thereof can be analysed. When high-energy electrons hit the specimen, they will excite core-level electrons. The following relaxation will generate characteristic X-rays that can be detected. The energy levels and the relative amounts of these X-rays can be detected. However, the drawback of this method is that it does not work for lighter elements (elements that are lighter than oxygen).

An Oxford Inca EDX system was used in this work. The accelerating voltage was set to 10 kV for the EDX measurements.

3.1.3. Fourier transform infrared spectroscopy

Infrared (IR) spectroscopy is a technique in which a sample is exposed to IR light and the absorption or transmittance is measured. The absorption is related to the resonance frequencies of bonds or groups that vibrate, i.e. it provides information on the bending and vibrational modes in molecules. IR spectroscopy can be used to detect the presence of known substances. It provides fingerprint spectra for metal oxides, particularly in the wavenumber region below 1100 cm^{-1}. In addition, IR spectroscopy is a non-destructive analysis method, and together with Fourier transform, it is a rapid technique. Fourier transform spectrometers do not use a monochromator to select each wavelength for scanning the region of interest. Rather, these spectrometers use an interferometer, which constructs an interferogram from waves travelling along paths of different lengths. The Fourier transformation of the data converts the information in the time domain to the frequency domain, thus considerably decreasing the time required for a single scan. The IR spectrum is generally in the range of 250 to 4000 cm^{-1}. Traditionally, an IR spectrum is recorded by passing the beam through a KBr pellet that contains the sample. The instrument used in this work was a Nicolet 6700 FT-IR with an optical range of 400 to 4000 cm^{-1}.

3.1.4. Raman spectroscopy

Raman spectroscopy is a technique for studying the vibrational, rotational, and other low-frequency modes in a system, and it provides a fingerprint by which molecules can be identified. Raman spectroscopy provides complementary information to IR spectroscopy. The physical difference between these two techniques is the criterion for a substance to be Raman active. The criterion is that the vibrational modes must correspond to a change in polarisability, which is not observed using the IR technique. Raman scattering occurs when laser light hits a sample and sends electrons to a virtual excited state. Most of the photons are elastically scattered (with no change in frequency). However, when an electron relaxes to a higher state than the ground state, it emits a photon that is lower in wavelength than the incoming laser, the so-called Stokes lines. The electrons can also relax to a lower energy level, providing increased energy to the emitted radiation, the so-called anti-Stokes. This process is shown in Figure 3.3 below.

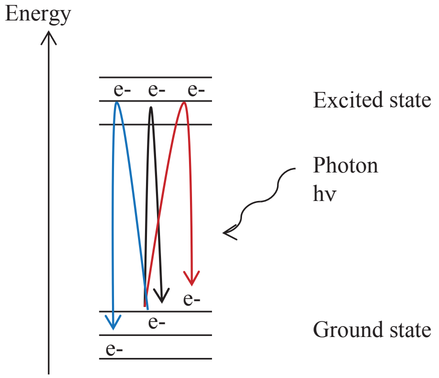

Figure 3.3 Principals of Raman scattering with elastic scattering (black line), Stokes scattering (red line) and anti-Stokes (blue line).

Raman spectra may be collected in the same range as IR spectra (200 to 4000 cm^{-1}). The technique is not particularly sensitive, but its sensitivity may be enhanced if the samples are coloured. In such cases, the excitation laser can be tuned to a real electronic transition, which is a technique called “resonance Raman spectroscopy”.

The Raman instrument used in this work was a Dilor XY800 Raman spectrometer with a Spectra-Physics tuneable Ar+/Kr+ laser. The spectrometer was operated with a holographic notch filter to reject excitation photons. A schematic of the setup is shown in Figure 3.4.

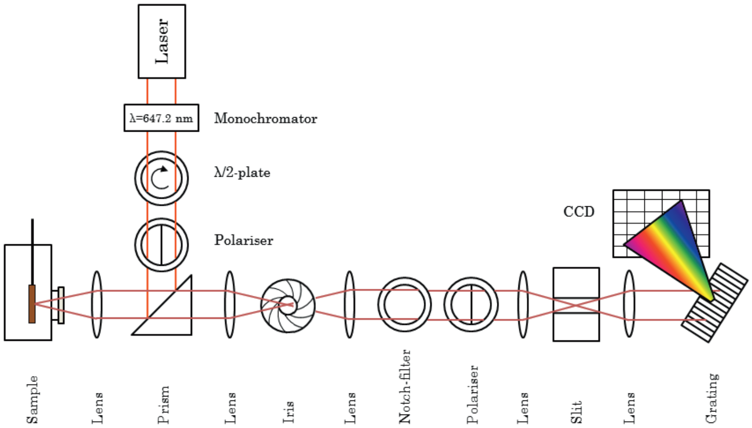
Laser
λ=647.2 nm
Monochromator
λ/2-plate
Polariser
CCD
Sample
Lens
Prism
Lens
Iris
Lens
Notch-filter
Polariser
Lens
Slit
Lens
Grating

Figure 3.4 Schematics of the Raman spectrometer used in this work.

3.1.4.1. *In situ* Raman spectroscopy

A strength of Raman compared to IR spectroscopy is that water is not strongly Raman active. This property affords the opportunity to investigate metal oxide surfaces in aqueous electrolytes. This unique character was utilised in this work. A special glass cell with a transparent quartz glass window was used for the measurements of the cathode surface while performing electrolysis. The experiments were performed in a back-scattering geometry with the sample located in the glass cell shown in Figure 3.5. The incoming light was focused on the working electrode inside the cell using a positive lens with a focal length of approximately 8 cm. The scattered light was collected through the same lens.

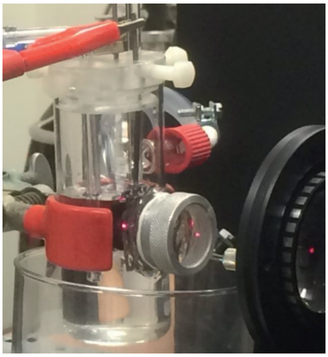

Figure 3.5 Photograph of the *in situ* Raman cell used in this work.

3.2. Electrochemical methods

Classical electrochemical methods such as linear sweep voltammetry and impedance spectroscopy are the foundation of this work. These methods are used to understand the system in detail. To transfer the results from these measurements into the relations for full-scale operation, a pilot plant was designed and constructed for “long-term” electrolysis and exposure to commonly found corrosive environments.

3.2.1. Electrochemical cell

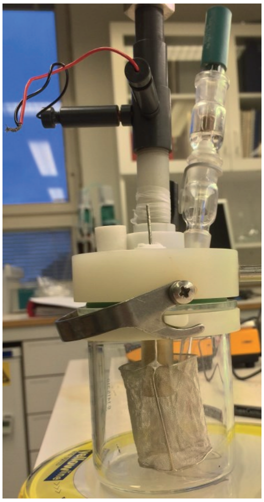

Figure 3.6 The three-electrode electrochemical cell used in the present work.

The electrochemical investigations were conducted using either a Gamry *Reference 600* or a Solartron *Electrochemical interface 1287* potentiostat. The cell was a single-compartment three-electrode cell. The working electrodes were disc electrodes hanging upside down, either stationary or rotating. The counter electrode was a cylindrical platinum net that surrounds the working electrode. The reference electrode was a double-junction Ag/AgCl (3 M KCl, E = + 0.210 V vs. NHE) electrode. The double junction was used to ensure that chlorides would not leak into the electrolyte.

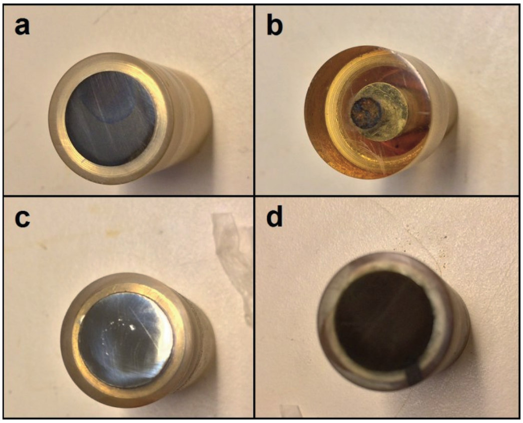

Figure 3.7 Examples of the electrodes used in this work. a) Titanium grade 1, b) carbon paste electrode with γ-FeOOH, c) mild steel and d) α-FeOOH electrodeposited on titanium grade 1.

Three types of working electrodes were used: mild steel, titanium and carbon paste. The mild steel electrode was a 1 cm^2 disc of Domex MS 21033 material from SSAB containing C <0.06 % C, 0.20-0.35 % Mn and <0.01 % S and is alumina sealed. The titanium electrode was also a 1 cm^2 disc made from titanium grade 1 containing <0.08 % C, <0.03 % C, <0.18 % C, <0.015 % H and <0.20 % Fe. The carbon paste electrode was 0.092 cm^2 and made of carbon paste from Metrohm and mixed with α- or γ-FeOOH powder, which were synthesised according to Schwertmann and Cornell [51].

3.2.2. Rotating disc electrodes

The rotating disc electrode ensures good hydrodynamic control. The rotational movement of the electrode drags the electrolyte to the surface. Because of the centrifugal force, the fluid is driven outward from the centre in a radial direction and fresh bulk electrolyte is “pumped” to the surface of the electrode, and the rotation velocity determines the flow rate, as shown in Figure 3.8.

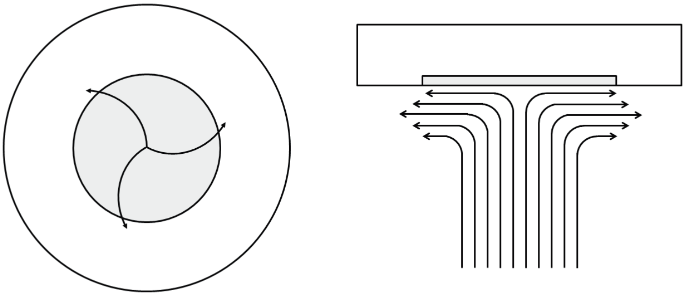

Figure 3.8 The hydrodynamic flow at a rotating disc electrode. The radial flow parallel to the surface to the left and the axial flow to the surface to the right.

There is also a diffusion-limited stagnant zone close to the electrode surface that decreases with increasing rotation speed. A model for the thickness of the diffusion layer (δ_O) has been derived by Levich [52], as shown in (23).

$$\delta_O = D_O / m_O = 1.61 D_O^{1/3} \omega^{-1/2} \nu^{1/6} \tag{23}$$

where D_O is the diffusion coefficient (cm^2 s^{-1}), m_O is the mass transfer coefficient (cm s^{-1}), ω is the rotation rate (rad s^{-1}), and ν is the kinematic viscosity (cm^2 s^{-1}). Since m_O is related to the limiting current (i_l) as in (24), it can be combined with (23) to provide the Levich equation (25).

$$m_O = i_l / nFAc_O^b \tag{24}$$

$$i_{l,c} = 0.62 nFAD_O^{2/3} \omega^{1/2} \nu^{-1/6} c_O^b \tag{25}$$

where A is the electrode surface area (cm^2) and c_O^b is the bulk concentration (mol cm^{-3}). However, the Levich equation is only valid at the limiting current plateau where the concentration of the reactants near the surface of the electrode is close to zero. To take the kinetic currents at low overpotentials into account, an expression has been formulated, the Koutecký-Levich equation (26) [52] for irreversible electron transfer reactions,

$$\frac{1}{i} = \frac{1}{i_k} + \frac{1}{i_{l,c}} = \frac{1}{i_k} + \frac{1}{0.62 nFAD_O^{2/3} \omega^{1/2} \nu^{-1/6} c_O^b} \tag{26}$$

where the kinetic current, i_k, is

$$i_k = nFAc^b k^0 \exp\left(-\frac{\alpha n F}{RT} \left(E - E^{0\prime} \right) \right) \tag{27}$$

From this relation, it is possible to calculate the kinetic constant, k^0, and the transfer coefficient, α.

3.2.3. Linear sweep voltammetry

The electrochemical technique that is generally adopted in combination with rotating disc electrodes is linear sweep voltammetry. This technique is performed by applying a linear potential scan on the working electrode in one direction, as shown in Figure 3.9, while continuously measuring the current. The results are visualised by plotting the current as a function of the applied potential. The measured current corresponds to the charging of the surface and to the electrochemical reactions occurring at the electrode.

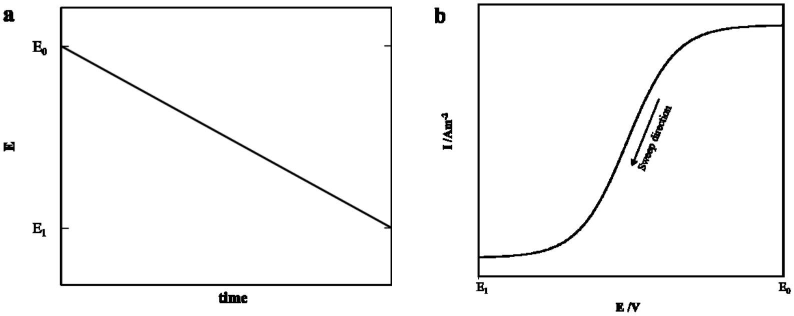

Figure 3.9 Potential profile vs. time for a linear sweep (a) and the corresponding measured current for a one-electron transfer reaction (b).

To obtain steady-state conditions and evaluate the kinetics of the reactions from linear sweeps, it is crucial to scan the surface at a slow rate. Higher sweep rates will introduce a transient response and increase the contribution of double-layer charging to the total current. Changing the potential at a rate of 5 mVs^{-1} is a good set point for kinetic studies. To follow the transitions in α- and γ-FeOOH, it was necessary to run analogue sweeps at rates as low as 0.1 mVs^{-1}. However, if the double layer or the capacitance is of interest, then it is not uncommon to have sweep rates up to 1000 Vs^{-1} (or even 10^6 Vs^{-1} for microelectrodes) [53].

3.2.3.1. Kinetic studies

Linear sweep voltammetry can be used to study the kinetics of an electrochemical reaction. Traditionally, the logarithm of the measured current (log *i*) is plotted versus the potential (or more generally, the overpotential). At low overpotentials, the potential versus log *i* is not linear due to back reactions, but at higher overpotentials, there is a true linear relationship between these parameters. The slope of the Tafel plot for a reduction reaction is then as follows:

$$\text{Tafel slope} = \frac{-\ln(10)\text{RT}}{\alpha \text{F}} \tag{28}$$

The transfer coefficient, α, is a symmetry factor that typically ranges from 0.2 to 0.8. This coefficient indicates whether the activated complex is closer to the product or the reactants. A one-electron transfer reaction at room temperature with $\alpha = 0.5$ presents a Tafel slope of 118 $mVdecade^{-1}$ [54]. Extending the Tafel slope down to zero for the overpotential reveals the exchange current density, i_0, from which the charge transfer resistance, R_{ct}, can be calculated.

$$R_{ct} = \frac{RT}{Fi_0} \tag{29}$$

In this work, kinetic modelling was used to evaluate the response from the linear sweeps. As shown in equation 27, the current is exponentially proportional to the potential. The currents from the experiments were fitted to the function to retrieve the transfer coefficient, α, and the kinetic constant, k^0. By knowing the magnitude of α, it is simple to calculate the Tafel slope from equation 28. With this method, the entire sweep is used for the evaluation, which will provide considerably more accurate results.

3.2.4. Electrochemical impedance spectroscopy

Electrochemical impedance spectroscopy (EIS) is a very powerful tool for evaluating the electric properties of a surface. The data evaluation is complex, but when performed properly, it is possible to discriminate between different processes occurring at the electrode. The impedance of the system is measured by introducing a small perturbation of the potential or the current passing through the system. This is facilitated by a sinusoidal AC wave, which is added to the static set point. By changing the frequency of the sinusoidal wave, it is possible to measure the impedance and phase angle shift of the response as a function of frequency. Scanning the frequency domain is generally performed by starting at high frequencies and moving to the lower frequency region. An electrochemical system that undergoes an AC perturbation can be viewed as an electrical circuit and modelled as such. For instance, if the phase shift is zero, then the impedance is a strict resistance. This is the case at very high frequencies, where the response corresponds to the solution resistance. A second extreme case is the -90° phase shift, which relates to a true capacitance, such as the double-layer capacitance. The entire system can therefore be investigated and characterised using the impedance technique. However, it is crucial to know what is being modelled to prevent overestimations, which will lead to good fits but with no physical meaning.

3.2.4.1. Controlled-potential EIS

Controlled-potential EIS is commonly used to study the electric properties of the electrode surface and the solution resistance. This technique can be performed either at open circuit potential or with a forced potential on the working electrode.

Impedance made at open circuit potential provides a view on the relaxed system. At high frequencies, the solution presents the highest response, and it is common to obtain a pure resistance in this case, which corresponds to the solution resistance. This resistance can be used to compensate for the applied potential in linear sweeps to obtain the true electrode potential. As the frequency is lowered, the electrode and the double layer close to it play larger roles and introduce capacitive effects.

When a forced potential is applied on the electrode, either in the positive or negative direction, an electrochemical process begins to occur. The charge transfer resistance, R_{ct}, can be estimated using impedance measurements. The charge transfer resistance will diminish with the sequential increase of the overpotential. From the relation between the applied potential on the electrode and the logarithm of the inverse R_{ct}, there will be a Tafel behaviour [55]. This behaviour is related to the steady-state current for the reaction occurring on the electrode.

3.3. Electrode preparation

Four main types of electrodes were used in this work: rotating disc electrodes, carbon paste electrodes, flag electrodes and pilot-plant-scale sodium chlorate cathodes. Depending on the physical appearance and use of the different electrodes, different preparation methods were used.

3.3.1. Rotating disc electrodes

Rotating disc electrodes was prepared from titanium grade 1 metal sheets and mild steel (DOMEX MS 21033). For this purpose, 1 cm^2 discs were lathed from the sheets and welded to a holder. The entire disc was then casted in an epoxy resin (Epofix, Struers).

When measured as pure metal substrates, the discs were polished with 4000 grit SiC paper from Struers and rinsed with 18 MΩ Milli-Q water. After polishing, the titanium discs were left in contact with air for 48 hours prior to testing to obtain stable and repeatable results. This step was performed to allow a stable and repeatable layer of oxides to form on the surface. The mild steel electrodes were used immediately.

3.3.1.1. Iron oxyhydroxide electrodes

The electrodeposition of iron oxyhydroxides on titanium substrates was used to produce the pure corrosion products for electrochemical investigations. Martinez et al. [56] reported a simple synthesis of α- and γ-FeOOH using only Mohr's salt and potassium acetate. This method was used as the basis for the synthesis. A rotating disc of titanium grade 1 was polished with 1000 grit SiC paper and rinsed with Milli-Q water. The electrolyte was prepared as described with 0.01 M Mohr's salt and 0.04 M potassium acetate, and it was kept under a nitrogen atmosphere at 90 °C. Only seconds prior to deposition, the titanium disc was etched with 5 % hydrofluoric acid for 10 seconds. Deposition was performed at -150 mV vs. Ag/AgCl (3 M KCl) for α-FeOOH and +1000 mV for γ-FeOOH. A total charge of 4 coulombs per cm^2 was used for the deposition. For the *in situ* Raman spectroscopy study, 2 cm^2 flag electrodes were prepared. These sets were only deposited with 2 coulombs per cm^2.

3.3.1.2. Chromium (III) deposition

Two different types of chromium (III) species were used in this work to obtain a deeper understanding into how chromium hinders the reduction of hypochlorite. The two different species are Cr_2O_3 and $Cr(OH)_3$, and they were deposited onto titanium rotating disc electrodes. The $Cr(OH)_3$ and Cr_2O_3 films were deposited from two different Cr(VI) solutions containing CrO_3, H_2SiF_6, $BaCO_3$ and KNO_3 with compositions as given by Aguilar et al. [57]. Deposition proceeded for 30 minutes at -1.60 V vs. Ag/AgCl. The electrodes were rinsed several times with Milli-Q water and stored immersed in Milli-Q water. The pre-treatment of the titanium discs was the same as that for the iron oxyhydroxide electrodes.

3.3.2. Flag electrodes

Pieces with dimensions of 2x1 cm were cut from titanium grade 1 sheets and welded to titanium rods with a diameter of 2 mm. The rods were covered with Teflon tape to maintain a flat and controlled surface area. Depositions of alpha and gamma iron oxyhydroxides were performed as previously described.

3.3.3. Carbon paste electrodes

For the studies of hydrogen evolution with vigorous gas evolution occurring on the working electrodes, carbon paste electrodes were used due to stability issues of the electrodeposited electrodes. α-FeOOH and γ-FeOOH powders were prepared as described by Schwertmann and Cornell [51]. The powders were ground in a mortar and mixed with carbon paste from Mettler-Toledo in a 40/60 (FeOOH/C) weight ratio. The carbon-iron mixture was pressed in a holder with a 3.2 mm diameter.

3.3.4. Pilot plant cell electrodes

A pilot plant was constructed to evaluate the electrode performance under "process-like" conditions, which will be discussed in Section 3.4. Electrode sheets with dimensions of 7x25 cm were mounted in the pilot plant cells. The electrodes were provided by Permascand AB and were PSC120 DSA for the anodes and Domex MS 21033 mild steel for the cathodes. The large sheets were cut into suitable sizes for the pilot cell using a water jet. The anodes were washed in 2 M HCl prior to their first use, and the cathodes were washed with deionised water and Jif (Unilever) hand-washing detergent.

3.4. Process-like conditions / pilot cell

A pilot plant was constructed to mimic the process and to investigate how different parameters in the sodium chlorate process affect the electrode performances and corrosion of the mild steel cathodes. The pilot plant provides the possibility for long-term exposure of the electrodes under either potentiostatic or galvanostatic conditions in sodium chlorate electrolyte. The great benefit of this equipment is that it follows the individual electrode current efficiencies while changing the operating conditions. Temperature, pH, salt concentrations, different additives, current densities, potentials and/or exposure time can be changed. This pilot plant was constructed from a combination of two parallel loops. In the main loop, the electrodes can be exposed under constant conditions for up to 6 months, while the second considerably smaller test loop is equipped with more instrumentation and gas analysis equipment for evaluating the performances of individual electrodes. The entire system is controlled by an ABB800 PLC (Process Logic Control) system. A schematic overview of the system is presented in Figure 3.10.

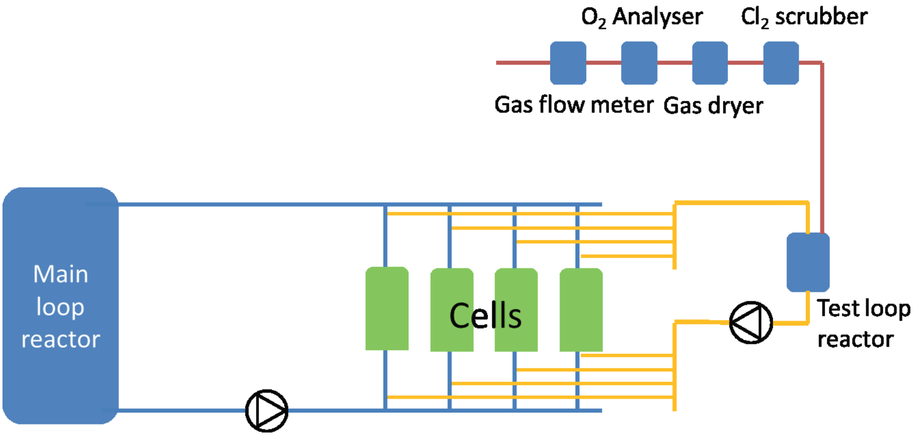

Figure 3.10 Schematic of the pilot plant used in this work.

The cell used in the plant, which is shown in Figure 3.11, was previously developed at AkzoNobel Pulp and Performance Chemicals for different setups.

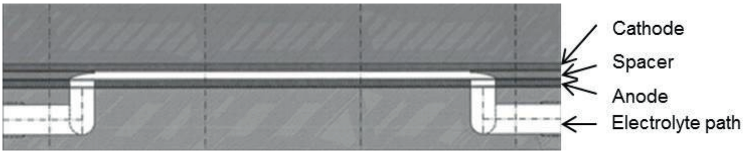

Figure 3.11 Cut through of the cells used in this work.

The main loop reactor is a stirred jacketed 200 dm^3 titanium vessel. It is heated with a Lauda heating bath, and it is equipped with a stirrer. From the reactor, 1” titanium piping leads to four parallel placed electrochemical cells. Fittings to the cells are composed of PVDF and PTFE. The circulation of electrolyte is enabled by an ABB centrifuge pump with a magnetic drive PVDF housing. A feedback flow meter to a frequency converter allows for control of the flows to maintain a laminar flow at 0.5 ms^{-1} of electrolyte over the electrodes. pH in the loop is controlled using a Mettler-Toledo InPro 4260i /SG pH electrode, and 2 M HCl was added to maintain a constant pH. An air flow of 3.6 m^3h^{-1} was purged into the reactor to dilute all formed hydrogen down to safe levels well under the explosion limit. To compensate for evaporation, all gasses were passed through a condenser, and a level monitor was connected to a pump to maintain a constant level with the addition of deionised water. All four cells were connected separately to individual rectifiers that can operate in either potentiostatic or galvanostatic mode.

A valve system allows each cell to be bypassed independently and connected to the smaller test loop without cutting the load on the cells. The test loop has a 0.7 dm^3 jacketed glass reactor heated with a Lauda water bath. pH control is the same as that in the main loop, but the cell gas handling system is different. Nitrogen can be added either by flushing large amounts or by controlled addition using a Brooks mass flow controller. The off gas is washed in 5 M NaOH to remove traces of chlorine and subsequently dried over silica gel. The clean and dry hydrogen and oxygen (and occasionally nitrogen) mixture is analysed for its oxygen content using a Servomex paramagnetic oxygen analyser, and the total flow is measured using a Brooks mass flow metre. The electrolyte circulation is generated by an Iwaki pump with a PVDF housing generating 150 dm^3h^{-1}.

3.4.1. Electrolyte

The electrolyte was produced from brine of recrystallised NaCl and commercial $NaClO_3$ crystals from the AkzoNobel chlorate plant in Stockvik, Sweden. The standard electrolyte composition was 110 gdm^{-3} NaCl and 590 gdm^{-3} $NaClO_3$, and the water used was deionised. Sodium dichromate (Fluka, reagent grade) and sodium sulphate (Merck, P.A.) were added in amounts to fit the experiments. The evaluated concentrations of sodium dichromate were 1, 3, 5 and 7 gdm^{-3}. Sodium sulphate was tested at fixed concentrations of 0, 5, 10 and 20 gdm^{-3}, while the concentration of sodium dichromate was maintained at 5 gdm^{-3}. The temperature effect was evaluated at four fixed values, 65, 68, 71 and 78 °C, with a fixed sodium dichromate concentration of 5 gdm^{-3} and zero added sodium sulphates. NaOH and HCl were added to maintain pH in the electrolyte and were of P.A. quality from Scharlau.

3.4.2. Method

For each test, a fresh cathode was used and operated under continuous operation for several days. During the test time, current interrupts were planned for 40 minutes each week to allow the cathode to corrode under these conditions. For various reasons, the plant’s safety system shut down the plant to avoid dangerous conditions, so-called trips. This led to some uncontrollable corrosion situations and is discussed in detail in Paper IV. Before the electrodes were removed, a run in the test loop was performed to evaluate the current efficiencies under these conditions and with the specific corrosion products on the surface. After the shutdown of the rectifiers, the cathodes were corroded for 40 minutes in circulating electrolyte in the main loop at open circuit potential before being removed from the cells.

4. Results and discussion

Worn mild steel cathodes were collected from two similarly constructed sodium chlorate plants and analysed in terms of current efficiency and surface composition. The identified corrosion products were later produced synthetically and analysed with respect to their electrochemical and physical properties. To investigate the surface during polarisation, i.e. under operation, *in situ* Raman was used. A pilot plant was constructed to test process parameters such as dichromate concentration, temperatures and sodium sulphate concentrations on a long-term scale. The correlation between the different corrosion products formed on the cathodes and how the current efficiency relates to the species were investigated. From the pilot plant study, optimal operating conditions can be formulated.

4.1. Study of sodium chlorate process cathodes

The study was started by selecting two sodium chlorate plants with different characteristics in terms of current efficiency. The two plants were built on the same technology: AkzoNobel PPC cylindrical cell boxes with multi monopolar electrodes [58]. Short-term trials had proved that the major difference in current efficiency was accounted for by the cathodes (Paper II).

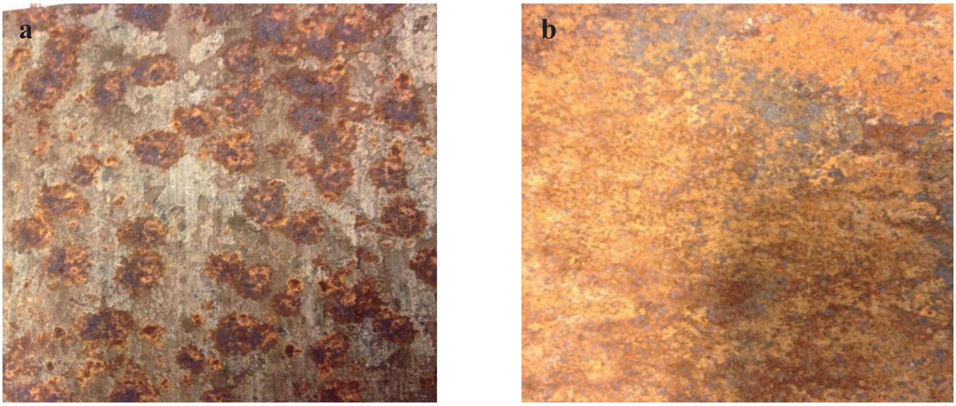

Figure 4.1 Photographs of two cathodes used from two different sodium chlorate plants, denoted Plant A (a) and Plant B (b) (Paper II supplementary).

The photographs in Figure 4.1 clearly show that the cathodes, which are both from mild steel, have corroded differently. Although the plants use the same technology, the operating conditions can still vary and influence the corrosion process of the cathodes. This result indicates that corroding an iron electrode in the presence of hypochlorite or taking an electrode from only a single plant will not provide a representative sample for a corrosion study of cathodes in the chlorate process. To evaluate the cathodic current efficiencies of the two cathodes, a test cell was used at AkzoNobel PPC [11]. The results from the test cell trials revealed that the cathode from Plant A reached a sufficiently high current efficiency in a couple of hours and slowly increased with time, whereas the cathode from Plant B did not even reach 88 % efficiency within the 6 hours for which the test was run. Because the difference in performance of the plants could be reproduced in laboratory tests, these two cathodes were chosen for further investigations in this work to determine which parameters are good or bad for the chlorate process relative to corrosion of the cathodes.

Both electrodes were investigated using SEM and EDX to detect any differences in composition, and XRD analyses were performed to identify the corrosion products. The SEM images presented in Figure 4.2 also show distinct differences between the two cathodes.

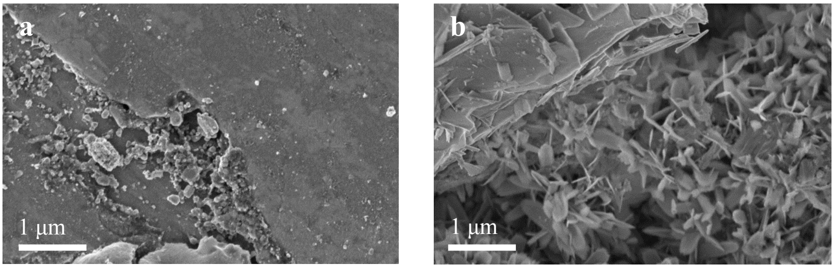

Figure 4.2 SEM images of electrodes from chlorate plants: Plant A (a) and Plant B (b) (Paper II supplementary).

The cathode from Plant B has a clear crystalline structure, shaped as thin flakes, whereas the one from Plant A does not show any large repeating structures. The XRD analysis presented in Figure 4.3 shows that the cathode from Plant A has a thin layer of goethite (α-FeOOH) on top and that the cathode from Plant B has a thick layer of lepidocrocite (γ-FeOOH). The thin layer of goethite is so thin that the majority of the signal corresponds to metallic iron in the steel underneath, whereas the lepidocrocite coverage is so thick that no substrate is visible.

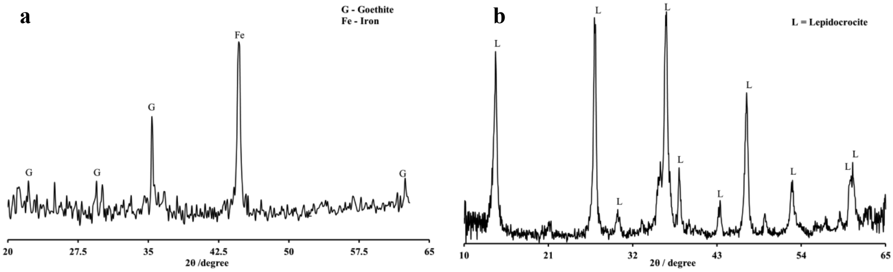

Figure 4.3 XRD analysis using Cu K_α radiation with a 5° incidence angle of the cathodes collected from Plant A (a) and Plant B (b) (Paper II supplementary).

4.1.1. Influences of operating conditions on the cathode corrosion

From the characterisation of the two cathodes in Section 4.1, it is easy to hypothesise that the two different iron oxyhydroxides have different electrochemical behaviours towards the two main reactions on the cathode: hydrogen evolution and hypochlorite reduction. This also leads to the hypothesis that the cathodes will corrode differently depending on the operating conditions in the plants.

4.1.1.1. Operating conditions for the extracted plant electrodes

Although the two plants were of the same technology and approximately the same size, their operating conditions differed. The differences in electrolyte composition and some of the plant operating conditions during the last month before shutdown and extraction of the cathodes from the process are shown in Tables 4.1 and 4.2. The information regarding the operating conditions and electrolyte compositions was provided as a courtesy by AkzoNobel PPC.

Table 4.1 Electrolyte compositions in gdm^{-3}.

	Plant A	Plant B
$NaClO_3$	587	602
NaCl	105	115
$Na_2Cr_2O_7$	4.2	5.9
Na_2SO_4	7.1	14.0
K	5.1	7.9
Fe	$1.8 \cdot 10^{-3}$	$3.3 \cdot 10^{-3}$

Table 4.2 Plant operating conditions.

	Plant A	Plant B
pH Cell	6.6	6.5
T Cell /°C	80	85
U Cell /V	2.86	2.94
I /kA	61	70-80
i /kAm^{-2}	2.5	2.6-3.0

Both plants are run within operating conditions generally employed for sodium chlorate plants [2, 9]. There is one distinct difference between the two plants, which is that all parameters are at a higher level in Plant B compared to Plant A except for the pH.

4.1.1.2. Laboratory-scale corrosion studies

To test the hypothesis that different operating conditions influence which corrosion product is formed, a master's project was set up to correlate the process parameters to the corrosion products that formed [59]. The tests were performed in a 1 dm^3 reactor filled with sodium chlorate electrolyte. A 2 cm^2 mild steel electrode was placed in an 8 cm^2 DSA cage to enable polarisation on both sides. The composition of the electrolyte and operating conditions were changed by varying the pH, temperature, dichromate levels and sulphate content.

The cathode was polarised for two hours to allow for the formation of the chromium film and to create a steady-state concentration of hypochlorite in the electrolyte. Then, the electrode remained unpolarised in the electrolyte overnight for the corrosion to proceed. The surfaces were analysed using SEM and XRD to characterise the corrosion products that formed.

Depending on the operating conditions, different corrosion products were formed on the cathodes. In addition to α-FeOOH and γ-FeOOH, β-FeOOH was also found, as well as some species of Fe_2O_3. Because the amounts of corrosion products that formed were rather low, it was difficult to draw clear conclusions regarding a correlation between the process conditions and the corrosion products that formed on the surfaces. However, there was a clear difference between the trials with sulphate compared to the ones without. With high amounts of sulphate (20 gdm^{-3}) in the electrolyte, lepidocrocite was the predominant phase. This result is also consistent with the result found for electrodes extracted from the plants. For Plant B, the sulphate concentration is twice as high as that in Plant A, as shown in Table 1.

Although the hypothesis of a correlation between the operating conditions and corrosion products on the cathode surface was validated in this work, more work is still necessary to fully elucidate this relationship. A more thorough study was conducted in the pilot plant unit, which operates for longer periods of time under more process-like conditions. In this unit, more corrosion products are formed on the surfaces, and the current efficiencies can also be measured *in situ* to correlate with the species that formed. The results from this study will be discussed later in Section 4.4.

4.1.2. Power consumption study on process cathodes

To verify that the cathodes removed from the process exhibit different characteristics during operation, a study was performed in the pilot plant. The current efficiencies and potentials were monitored during the start-up procedure, and the time dependence was evaluated.

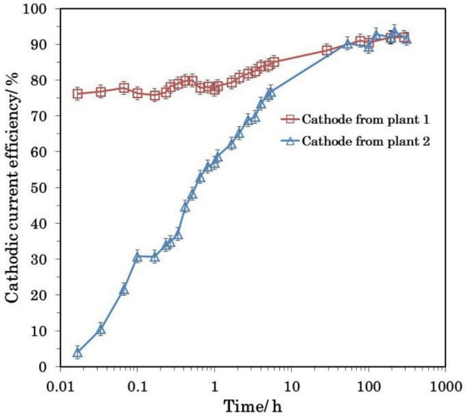

Figure 4.4 Current efficiencies of the sodium chlorate process cathodes collected from two different plants when starting under the same conditions in a pilot unit (Paper IV).

It is clear from Figure 4.4 that the cathodes from plant B show extremely poor performance during start-up. Not until two full days of operation the efficiency of the cathode from Plant B approach the same value as the better performing cathode from Plant A. Integrating the efficiency loss during the first 53 hours of a start-up leads to an average current efficiency loss of 7.1 %. To put this number into a larger context, a calculation of the difference in power consumption during the start-up period was performed. The calculations were based on an average sodium chlorate plant with an annual production capacity of 50 thousand tons. If the poorly performing cathode is used, each start-up will then have an increased power consumption of 351 000 kWh during the first 200 hours compared to operating conditions during steady state. Using the average energy cost for industrial consumers in EU 2015 [60], this corresponds to a difference of 10 k€ per start-up with a poorly performing cathode.

4.2. Kinetic investigations on α- and γ-FeOOH

To conduct a detailed study on the two differently behaving corrosion products, the goethite and the lepidocrocite were both synthesised in their pure forms and investigated with respect to their kinetics towards hypochlorite and water reduction.

4.2.1. Synthesis and stability of α- and γ-FeOOH phases on electrodes

Two different types of electrodes were produced for the kinetic trials: an electrodeposited rotating disc electrode (Section 3.3.1.1) and a carbon paste electrode with the corrosion product mixed with an inert carbon paste (Section 3.3.3). For the electrodeposited rotating disc electrodes, a preferred orientation of the iron oxyhydroxide phases was found. This preferred orientation was occasionally quite excessive, as shown in Figures 4.5 C and D, for the γ-FeOOH but not to the same extent for the alpha phase. To prove that the correct phase was deposited on the electrode, the gamma phase was removed from the surface and examined as a powder in the diffractometer. This result is shown as # in Figure 4.5. The alpha phase also showed some tendencies for preferred orientation but not to the same extent as for the gamma phase. These results and conclusions were also observed in previous work from Martinez et al. [56] when working with the method development.

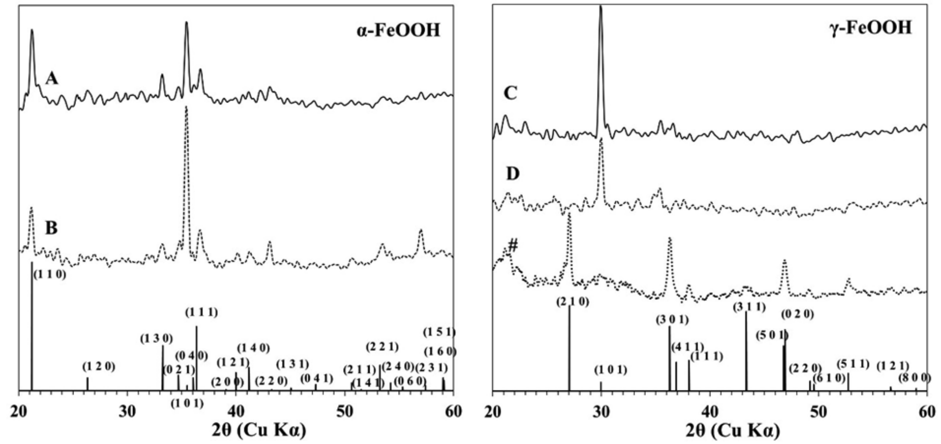

Figure 4.5 X-Ray diffractograms of pristine α-FeOOH (A) and α-FeOOH after 900 s at -1.2 V vs. Ag/AgCl (B), pristine γ-FeOOH (C) and γ-FeOOH after 900 s -1.2 V vs. Ag/AgCl (D). Reference diffractograms are shown in the bottom, and XRD pattern for removed material from deposited γ-FeOOH is shown in # (Paper II).

Stability tests were performed on the electrodes to ensure that no phase transition occurs during the kinetic study of hypochlorite reduction. For the trials with hypochlorite reduction, it was decided to stop the sweep in the negative direction at -0.8 V vs. Ag/AgCl. There were two reasons for this decision: the first was that a limited amount of redox current is observed on the surface, as shown in Figure 4.6, and the second is that the kinetic current flowing during hypochlorite reduction was sufficiently large for the study; see Section 4.2.2 for further details.

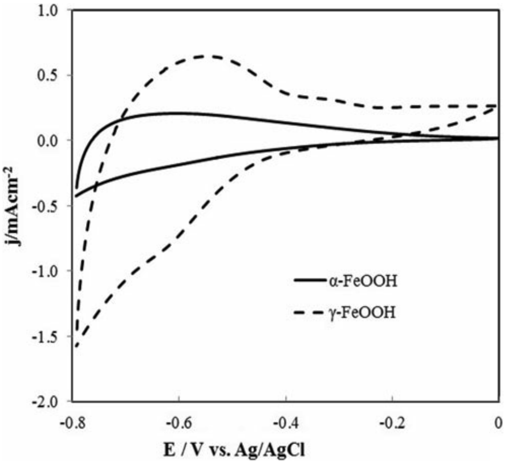

Figure 4.6 Background sweeps performed in 0.200 M Na_2SO_4 with pH 11 at 25 °C on rotating disc electrodes electrodeposited with α-FeOOH and γ-FeOOH. The rotation rate was 3000 rpm, and the sweep rate was 5 mVs^{-1} (Paper I).

The stability of the electrodeposited species was evaluated in two different ways: both with and without hypochlorite in the electrolyte. The electrodes were characterised using XRD to verify any changes in the iron phases that occurred during the kinetic trials with hypochlorite reduction. As shown in Figure 4.7, the stability of the phases was good, and they remained intact during the trials. The immersion in hypochlorite containing electrolyte and the potential sweeps performed on the electrodes did not affect the morphology or the oxidation state of the corrosion deposits. SEM images are also incorporated here to visualise the differences between the two different phases. The gamma phase, lepidocrocite, which is shown in the bottom right of Figure 4.7, exhibits typical flake-like crystals on a homogenous surface. The SEM images for the alpha phase, goethite, which are shown in the bottom left of Figure 4.7, show a completely different surface. This surface is coarser with no well-defined crystals.

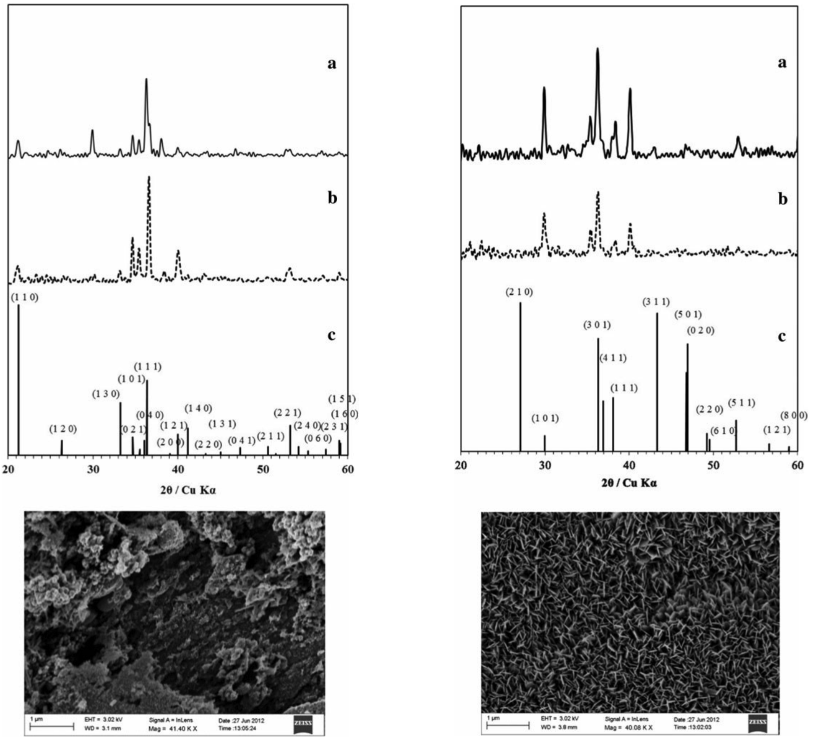

Figure 4.7. α-FeOOH (left) and γ-FeOOH (right) deposited on titanium substrates. XRD analysis of the electrodes before (a) and after the experiments (b). (c) The standards (PDF 00-029-0713 for α-FeOOH and PDF 00-044-1415 for γ-FeOOH) and the SEM images of the electrodes (shown below) (Paper II).

To study the kinetics of the HER, the potential sweeps were performed at a more negative potential. Linear sweeps were therefore performed down to -1.8 V vs. Ag/AgCl in 0.200 M Na_2SO_4 electrolyte at pH 11 to test the stability of the electrodes under hydrogen evolution. The sweep rate was 5 mVs^{-1}, and the rotation speed was 3000 rpm. The potential sweep for α-FeOOH shows a small reduction current before the hydrogen evolution occurs at approximately -1.4 V vs. Ag/AgCl, as shown in Figure 4.8 a. The γ-FeOOH sample presents a large reduction peak at -1.25 V before the hydrogen evolution begins. The potential for hydrogen evolution coincides for the two different corrosion products. To further investigate these reduction currents, the electrodes were placed under potentiostatic conditions at -1.2 V vs. Ag/AgCl for 900 seconds. The currents and total cumulative charge can be followed in Figure 4.8 b. In the long-term perspective, one can observe an opposite effect of the two electrodes than what would be expected from the linear sweeps. The high starting reduction current on the γ-FeOOH is quickly diminished and is almost zero after 900 seconds. For the alpha phase, the current is continuously increasing over time. This leads to a total of four times more charge running in the alpha phase compared to the gamma phase.

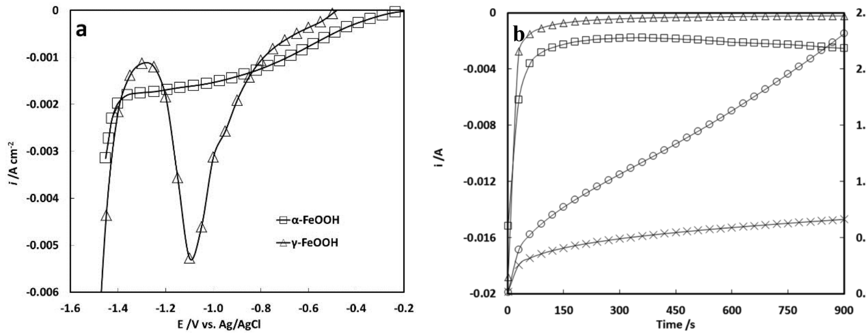

Figure 4.8 Linear sweep voltammetry (a) in the negative direction at 5 mVs^{-1} for α-FeOOH (□) and γ-FeOOH (△) in 0.2 M Na_2SO_4 at pH 11. (b) Current and total charge during potentiostatic load at -1.2 V vs. Ag/AgCl for α-FeOOH (□ for current and ○ for charge) and γ-FeOOH (△ for current and × for charge) (Paper II).

XRD analyses of the surfaces were also performed before and after these tests. No change in the surface composition could be detected, as shown in Figure 4.5. The reduction of FeOOH has been discussed in the literature, and it has been proposed that it is reduced to $Fe(OH)_2$ [61-64]. $Fe(OH)_2$ is highly reactive in air and will be oxidised to trivalent iron. See the discussion in Section 4.4. The reduced species are oxidised back to their original form when removed from the electrolyte. However, the electrodes were unstable during hydrogen evolution and the deposits fell off. Carbon paste electrodes with the desired oxyhydroxide species were therefore used during the kinetic study of hydrogen evolution.

4.2.2. Kinetics of hypochlorite reduction

As the first step towards understanding the differences between α-FeOOH and γ-FeOOH, the kinetics of the reduction of hypochlorite was investigated. As previously discussed, hypochlorite is an intermediate in the chlorate process. Together with its acid form, it forms the reactants for the wanted disproportionation to chlorate. However, hypochlorite is relatively unstable and can be oxidised to chlorate and oxygen on the anode, decompose in the electrolyte to chlorides and oxygen and can be reduced on the cathode, which is the main loss reaction in the sodium chlorate process. Hence, investigating the kinetics of the hypochlorite reduction on the pure iron oxyhydroxide species is essential to understand the role of different corrosion products in terms of performance. Sodium dichromate is added to the electrolyte to reduce the unwanted reactions, particularly on the cathode, and promote the disproportionation reaction. On the cathode, chromium (VI) is reduced to a chromium (III) film, which efficiently hinders the reduction of hypochlorite while allowing the hydrogen evolution to proceed [15, 16, 31].

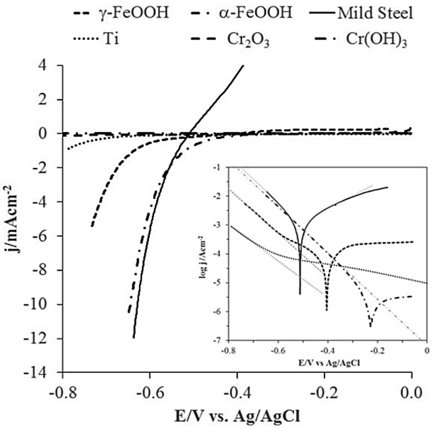

Figure 4.9 Linear sweeps of hypochlorite reduction at different substrates in 0.2 M Na_2SO_4 with 70 mM NaClO at pH 11. In the inset, the logarithm of the current density is plotted as a function of potential for Ti, α- and γ-FeOOH, and mild steel as substrates. The grey lines show the fittings to a one-electron transfer reduction. For mild steel, an anodic reaction was also included in the simulation. The sweep rate was 5 mVs^{-1}, and the rotation rate was 3000 rpm (Paper I).

α-FeOOH and γ-FeOOH were deposited on polished titanium discs prior to the tests. Mild steel was used for comparison with a fresh cathode, and a titanium disc was used to verify that the response came from the deposited iron oxyhydroxides and not the substrate. As shown in Figure 4.9, the Fe(III) oxyhydroxides do not react further as there are no oxidation currents. Conversely, mild steel behaves differently from the oxyhydroxides by showing a kinetic corrosion current at potentials that are more positive than -0.510 V, whereas the hypochlorite reduction is dominating at more negative potentials. Mild steel is also observed to be the most active substrate towards hypochlorite reduction, followed by α-FeOOH, γ-FeOOH and finally titanium. For comparison, the sweeps for chromium (III) oxide/hydroxide are included, showing no activity towards hypochlorite reduction. The current at -0.6 V is one order of magnitude lower for the gamma phase and two orders of magnitude lower for titanium than for mild steel and the alpha phase, as shown in Table 4.3.

Table 4.3 Kinetic data for hypochlorite reduction [ClO$^-$] =70 mM, pH = 11 (Paper I).

	j/mAcm^{-2} at -0.6 V	α	Slope/mVdec^{-1}
Ti	0.05	0.37	158
Mild Steel	4.27	0.47	125
α-FeOOH	3.98	0.47	124
γ-FeOOH	0.46	0.45	130

The logarithm of the linear sweeps for titanium and the iron oxyhydroxides were fitted to an irreversible one-electron transfer reaction (equation 27), while for the mild steel, it was necessary to also include the anodic electron transfer to take the corrosion process into account. The simulations are shown in the inset of Figure 4.9. The Tafel slopes are approximately the same for the three different iron electrodes with 120 mV per decade for the reduction of hypochlorite. With transfer coefficients, α, close to 0.5, it shows that the first electron transfer is rate limiting. It is also observed that the first electron transfer is rate limiting for titanium, but the transfer coefficient is slightly smaller, and the Tafel slope is 160 mV per decade.

4.2.3. Hydrogen evolution kinetics

The hydrogen evolution kinetics was studied on the two different iron oxyhydroxide phases and was compared with pristine freshly polished mild steel. Figure 4.10 presents three consecutive studies on mild steel, α-FeOOH and γ-FeOOH. The studies were performed in the order of linear sweep voltammetry, steady-state current measurements with potential steps and a following second linear sweep voltammetry. The resulting Tafel plots presented in Figure 4.10 show that both α- and γ-FeOOH exhibit the same low activity towards the HER on the first sweep. The activity changes with time, and during steady-state measurements, the activity is the same as that for mild steel. Even the linear sweep performed after the steady-state study showed that the improved activity was maintained.

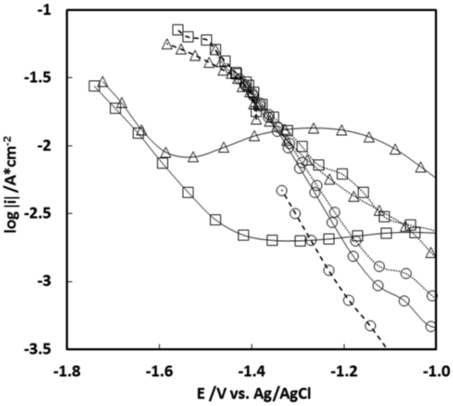

Figure 4.10 Currents versus potential for linear sweeps on steady states of mild steel (○), α-FeOOH (□) and γ-FeOOH (△) electrodes before (——), during (– – –) and after (·····) steady-state current measurements (Paper II).

The evaluated kinetic data, including rate constant, transfer coefficient and Tafel slope, are shown in Table 4.4. It is clearly observed in Table 4.4 that there is a one order of magnitude difference between the kinetic constant for the oxidised iron species and that for the pristine mild steel.

Table 4.4 Rate constant (k1), transfer coefficient (α) and corresponding Tafel slopes modelled for α-FeOOH, γ-FeOOH and mild steel. Values are calculated from linear sweeps of pristine material (Ls 1), after polarisation (Ls 2), steady-state currents (i_{ss}) and the charge transfer resistance (R_{ct}) (Paper II).

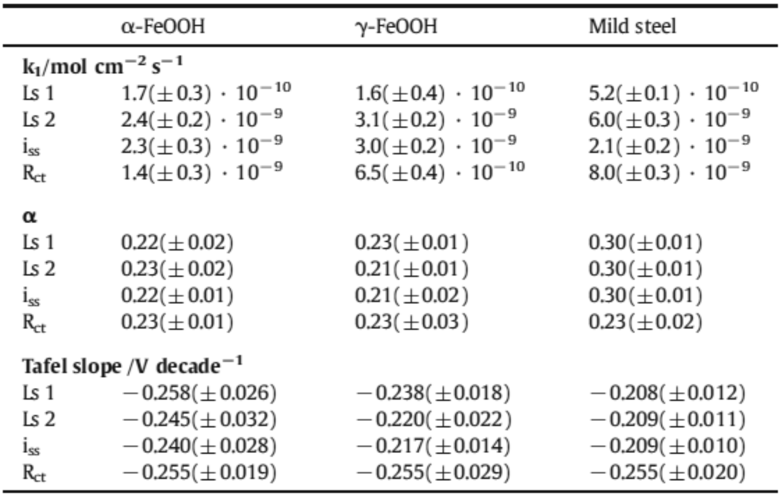

	α-FeOOH	γ-FeOOH	Mild steel
k_1/mol cm^{-2} s^{-1}			
Ls 1	$1.7(\pm 0.3) \cdot 10^{-10}$	$1.6(\pm 0.4) \cdot 10^{-10}$	$5.2(\pm 0.1) \cdot 10^{-10}$
Ls 2	$2.4(\pm 0.2) \cdot 10^{-9}$	$3.1(\pm 0.2) \cdot 10^{-9}$	$6.0(\pm 0.3) \cdot 10^{-9}$
i_{ss}	$2.3(\pm 0.3) \cdot 10^{-9}$	$3.0(\pm 0.2) \cdot 10^{-9}$	$2.1(\pm 0.2) \cdot 10^{-9}$
R_{ct}	$1.4(\pm 0.3) \cdot 10^{-9}$	$6.5(\pm 0.4) \cdot 10^{-10}$	$8.0(\pm 0.3) \cdot 10^{-9}$
α			
Ls 1	0.22(±0.02)	0.23(±0.01)	0.30(±0.01)
Ls 2	0.23(±0.02)	0.21(±0.01)	0.30(±0.01)
i_{ss}	0.22(±0.01)	0.21(±0.02)	0.30(±0.01)
R_{ct}	0.23(±0.01)	0.23(±0.03)	0.23(±0.02)
Tafel slope /V $decade^{-1}$			
Ls 1	−0.258(±0.026)	−0.238(±0.018)	−0.208(±0.012)
Ls 2	−0.245(±0.032)	−0.220(±0.022)	−0.209(±0.011)
i_{ss}	−0.240(±0.028)	−0.217(±0.014)	−0.209(±0.010)
R_{ct}	−0.255(±0.019)	−0.255(±0.029)	−0.255(±0.020)

The first pristine sweep performed on the FeOOH species with the lower kinetic constants is consistent with Figure 4.10. After reduction of the surface, the kinetics of all three surfaces are similar. It is also observed that all three different techniques that were used present similar results. The transfer coefficient, α, is approximately 0.2 to 0.3, which indicates that the activated complex on the surface is shifted towards adsorbed hydrogen rather than water in solution.

4.2.4. Concluding remarks regarding kinetic studies

By combining the results from the kinetic studies and the stability study, shown in 4.2.1, the following conclusions can be drawn. Both of the iron oxyhydroxide phases, α-FeOOH and γ-FeOOH, have poor performance towards hydrogen evolution, but both of these phases are still active for hypochlorite reduction. However, the iron oxyhydroxide surface is observed to be reduced and thereby becomes more active towards hydrogen evolution, reaching a state identical to that found on mild steel. It is proposed that the active phase on the surface of the cathode is $Fe(OH)_2$ because reduction to Fe(0) is not possible in aqueous solution. The rate of reduction for the two different iron oxyhydroxides is also shown to be different and is believed to be the reason for why the two different process cathodes show different current efficiencies.

4.3. *In situ* Raman studies of the reduction of α- and γ-FeOOH

As mentioned in Section 4.2.1, the active species under hydrogen evolution on mild steel is believed to be $Fe(OH)_2$. These results are based on indirect methods or *ex situ* analyses of surfaces [61, 63-67]. To identify the active compound under polarisation, an *in situ* Raman spectroscopy study was performed. This investigation was performed by studying the surface while gradually lowering the potential.

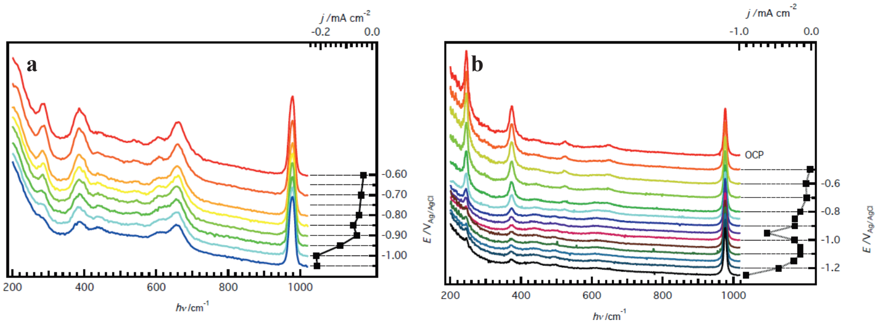

Figure 4.11 The evolutions of Raman spectra with increasing cathodic load for α-FeOOH (a) and γ-FeOOH (b) using a wavelength of 647 nm together with the steady-state currents for each potential (Paper III).

As the potential was shifted towards more negative potentials, the Raman signals related to the oxyhydroxides diminished, as shown in Figure 4.11. The shape of the corresponding steady-state currents versus potential is similar to the linear sweep presented in Figure 4.8 a, although at this slow change in potential, the surface is reduced and hydrogen evolution begins at less negative potentials. The features in the Raman spectra were maintained during the first plateau where only charging currents occur, i.e. no faradaic process. When reaching the potential where the reduction of FeOOH occurs, the Raman signal for the FeOOH species started to disappear. The sulphate peak at approximately 981 cm^{-1} was maintained and was therefore used for verification of the true signal strength.

Since the overpotential for hydrogen evolution was lower in these steady-state measurements than for the linear sweeps, it was interesting to determine what occurs during the linear sweeps when they are performed at an extremely slow rate. Figure 4.12 presents linear sweeps performed on goethite and lepidocrocite using an analogue potentiostat at a sweep rate of 0.1 mVs^{-1}.

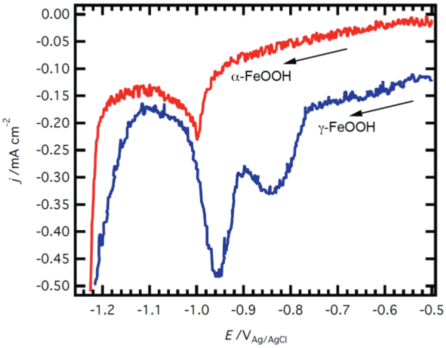

Figure 4.12 True analogue linear sweeps performed on α-FeOOH and γ-FeOOH in the cathodic direction with a sweep rate of 0.1 mVs^{-1} (Paper III).

Comparing Figure 4.12 with Figure 4.8 a reveals some similarities as well as significant differences. In the study shown in Figure 4.8 a, the sweep rate was 5 mVs^{-1}, and only a part of the surface transitions occurred. At the low sweep rate, 0.1 mVs^{-1}, the phase transition of the surface is complete and hydrogen evolution starts at potentials similar to those in the steady-state trials of the kinetic study for the reduced species, as shown in Figure 4.10. Figure 4.12 shows that there is a reduction peak for the alpha phase at approximately -1.0 V vs. Ag/AgCl, whereas for the gamma phase, there is a two-step process starting at -0.8 V and a following second process at -0.94 V vs. Ag/AgCl. The interpretation of this slow kinetics is that it is a solid-state reduction process that is mass transport limited within the material itself.

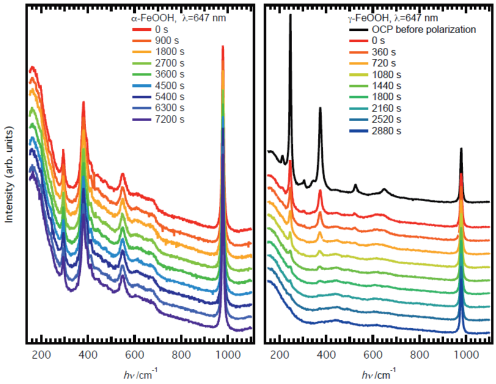

Figure 4.13 Time dependence of Raman spectra during polarisation of -950 mV vs. Ag/AgCl for α-FeOOH and γ-FeOOH using a laser wavelength of 647 nm, as indicated (Paper III).

Keeping the two different FeOOH species at a constant negative potential of -950 mV vs. Ag/AgCl for longer periods of time verifies that the gamma phase is readily reduced at this potential while the alpha phase is only partially reduced, as shown in Figure 4.13. This result is expected since this potential is at the top of the peak current for the gamma phase while only at the beginning of the reduction of the alpha phase.

The disappearance of the Raman signal does not indicate what is formed on the surface. The previously performed XRD study, shown in Figure 4.7, did not show emerging peaks corresponding to solid iron after reduction of the surfaces, leading to the conclusion that the reduced species must be divalent iron with no or at least a very low Raman signal. An additional trial with a green laser at 514 nm was performed to determine whether there were shifts in the Raman resonance, but no change was observed. Low Raman signals for $Fe(OH)_2$ have been reported in the literature [68, 69]. Odziemkowski et al. [68] even used surface-enhanced Raman scattering by depositing a discontinuous silver film on top of the surface. A different approach was used here by measuring the re-oxidation of the surface after the reduction was performed. As shown in Figure 4.14, spectra were collected at different times during the spontaneous re-oxidation of γ-FeOOH. Spectrum (1) shows the native electrode at open circuit potential in the electrolyte prior to reduction. Spectrum (2) shows the electrode at the end of the polarisation sweep. The electrode was then removed and rinsed in water before being measured again, yielding spectrum (3). The electrode after one night of exposure to air at ambient temperature presented spectrum (4). Finally, the electrode was rinsed once more in water, producing spectrum (5).

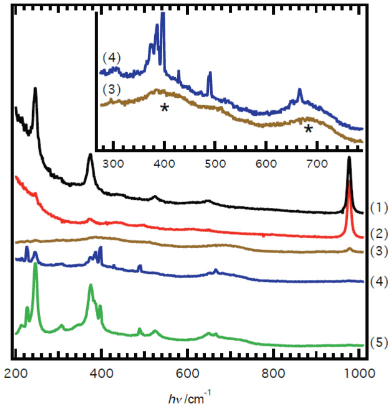

Figure 4.14 Re-oxidation of γ-FeOOH on titanium substrate, where (1) is the fresh surface under open circuit potential. Spectrum (2) shows after reduction, (3) is after the sample is removed from the cell and rinsed with Milli-Q water. Spectrum (4) is after one night in air, and finally, (5) is after a second rinse in Milli-Q water. The inset shows spectra (3) and (4) at different scales (Paper III).

The most important peaks are observed in the inset in Figure 4.14. In spectrum (3), two broad peaks are marked with asterisks. The spectrum was collected immediately after the reduced sample was rinsed and exposed to air. These peaks were attributed to δ-FeOOH, which is isostructural to $Fe(OH)_2$ [70, 71]. δ-FeOOH is a poorly crystalline phase that will undergo a transformation to the alpha or gamma phase depending on the pH and electrolyte composition. The presence of δ-FeOOH in the re-oxidation from Fe(II) supports that $Fe(OH)_2$ is formed under cathodic polarisation.

4.4. Studies on the effects of dichromate in the chlorate process

4.4.1. Sodium dichromate and cathodic current efficiency

The first effect investigated was the CCE. As previously mentioned in Section 2.4, sodium dichromate has been used since the late 19th century and has an important impact on the efficiency of the process. Several studies have been conducted to understand the role of sodium dichromate, but the exact mechanism is not yet fully established [8, 11, 15, 16, 22, 28, 30, 31, 33, 45, 46]. Wulff and Cornell [11] showed that there is a concentration dependence on the current efficiency with respect to dichromate concentration. Their experiments were performed for a rather short time, and the chromium film did not fully develop during their experiments. The film is still developing even at longer time scales, up to 9000 s, as shown by Ahlberg Tidblad and Mårtensson [32]. In the pilot study presented in Paper IV, the timescale is over several days to reach the steady state of chromium film formation.

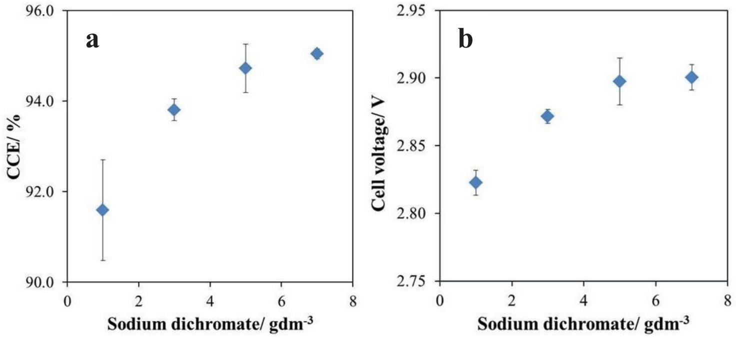

Figure 4.15 Current efficiency (a) and cell voltage (b) at steady state in the sodium chlorate pilot unit with respect to the concentration of sodium dichromate (Paper IV).

Figure 4.15 shows the large effects that sodium dichromate has on the process between 1 and 5 gdm^{-3}. The more dichromate that there is in the electrolyte, the higher are the current efficiency and cell voltage. At concentrations above 5 gdm^{-3}, there is little or no further change in the effect on either current efficiency or cell voltage with increased concentration of chromate. This result can be interpreted as how the thickness of the formed trivalent chromium film on the cathode is concentration dependent up to 5 gdm^{-3}. A concentration dependence on the thickness of the chromium (III) film was shown by Ahlberg Tidblad et al. [32]. Furthermore, the selectivity (its inhibiting effect on hypochlorite and chlorate reduction) appears to be dependent on the film thickness.

To understand the mechanism responsible for the chromium film behaviour compared to the corroded steel surface, a theoretical calculation was conducted, as reported in Paper I. Density functional theory (DFT) calculations were performed to determine the energy required for the reduction of hypochlorite on chromium (III) and iron (III) species, as in Paper I. The DFT calculations, which used adsorbed chlorides as a descriptor, revealed that there is no difference in the electrocatalytic properties for trivalent iron and chromium oxides. However, the experimental study of chromium (III) deposited on titanium as Cr_2O_3 and $Cr(OH)_3$ did indicate that the chromium species completely block the hypochlorite reduction process, as shown in Figure 4.9. These results along with the results from the process make it plausible to conclude that the electronic properties of the chromium film provide cathodic selectivity. Iron oxides and iron oxyhydroxides are known for their n-type semiconducting properties, thus making them good materials for reduction reactions. Conversely, chromium (III) oxides are known to be p-type semiconductors, which efficiently hinder reductions. Therefore, it appears that the p-type chromium (III) film located on the surface of the cathode is hindering reduction reactions from occurring but is still allowing water to pass through to the cathode substrate for reduction. In other words, this film functions as a sieve, hindering hypochlorite and chlorate from reaching the active cathode surface and thereby increasing the current efficiency. With corroded cathodes, there will be a mixture of n- and p-type semiconductors on the surface where more iron than chromium will impart the surface with n-type characteristics [72]. This situation results in the need for more dichromate in the electrolyte to increase the current efficiency.

4.4.2. Sodium dichromate and oxygen evolution

Oxygen evolution in the chlorate cell is a concern not only due to safety reasons (mixing with hydrogen) but also since it is a direct current efficiency loss. As shown in Figure 4.16, there is a linear response between the molar formation of oxygen in the cell gas and the concentration of sodium dichromate in the electrolyte. Colman [9, 73] reported that sodium dichromate in the electrolyte reduces the oxygen concentration in the cell gas. Hardee and Mitchel [22] did not show a decreasing trend in the oxygen content in the cell gas with their experimental results, although they state that full-scale plant data would support such a trend. However, there are some contradictory results in the literature from Nylén et al. [74] and Spacojevic et al. [28] regarding anodic oxygen formation. Additionally, Sandin et al. [75] did not observe any effect of chromate on either chlorate formation or oxygen evolution; however, very low chromate concentrations were used.

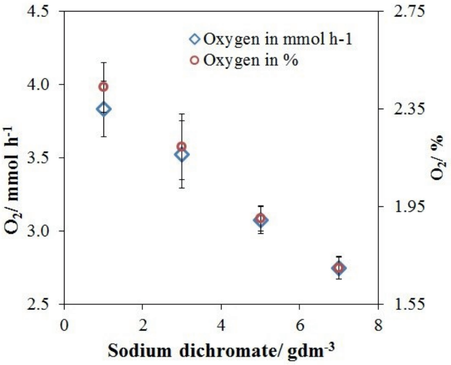

Figure 4.16 The oxygen content in the cell gas from a sodium chlorate pilot cell during normal operating conditions with respect to the concentration of sodium dichromate in the electrolyte. The oxygen is presented both as molar formation and as percentage in the cell gas (Paper IV).

The linear decrease in oxygen formation with increasing concentration of sodium dichromate in the electrolyte supports the discussion of its catalytic properties for the homogeneous chlorate formation reaction. There is also no minimum for the total power consumption; the oxygen formation is steadily decreasing in the interval tested. Extensive studies conducted by Wanngård [76] showed that the majority of this effect is attributed to the catalytic property that sodium dichromate has on the chlorate formation reaction (Equation 6 in Section 2.1). However, since the CCE does not continue to significantly increase above 5 gdm^{-3}, the total power consumption will not continue to decrease at the same rate when more dichromate is added. This concentration may consequently be considered a pseudo-optimal concentration.

4.4.3. Stability of the chromium (III) film

To estimate the stability of the chromium (III) film during shutdown, the open circuit potential was measured and complemented with an EDX analysis of the surface. The power was shut down, and the electrodes were kept in hypochlorite containing electrolyte for 40 minutes to corrode. The open circuit potential during this period did not increase above -0.1 V vs Ag/AgCl, as shown in Figure 4.17.

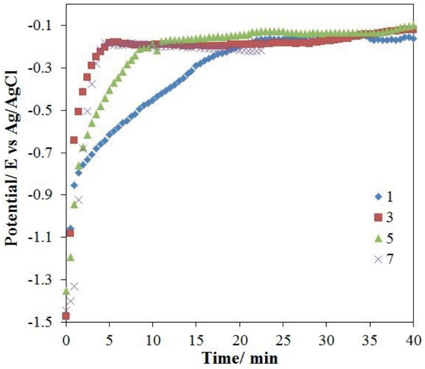

Figure 4.17 Open circuit potential measurements of mild steel cathodes operated at 2 kAm^{-2} for several days in sodium chlorate electrolyte. The electrolyte was 110 gdm^{-3} NaCl, 580 gdm^{-3} $NaClO_3$ and the levels of sodium dichromate varied between 1 and 7 gdm^{-3} at 71 °C (Paper IV).

The potential for the oxidation of $Cr(OH)_3(s)$ to CrO_4^{2-} is approximately 0.45 V vs. Ag/AgCl at pH 6.8 and 71 °C. This potential is considerably higher than the -0.2 to -0.1 V measured in this study. A conclusion is therefore drawn that the chromium (III) film on the cathode surface is not oxidised during these 40-minute shutdowns. This conclusion is further supported by the EDX analyses of the surfaces, which reveal substantial amounts of chromium remaining on the surface even after several washing steps, as shown in Table 4.5. It is hypothesised that the corrosion process that is occurring corresponds to the oxidation of Fe(II) to Fe(III) underneath the chromium film.

Table 4.5 EDX analyses of surfaces of mild steel cathodes run with different amounts of dichromate in the electrolyte (Paper IV).

Element	at% 3 gdm^{-3}	at% 5 gdm^{-3}	at% 7 gdm^{-3}
Cr	17.6	17.9	20.0
Fe	20.5	4.8	5.6
O	45.7	49.8	52.7
Cl	0.8	5.7	2.4
Ag	0.2	0.3	0.9
C	10.8	8.9	7.5
Ca	0.6	6.4	4.9
Mg	1.0	2.2	3.1
Na	0.7	1.8	1.1
Si	1.1	0.3	0.3
Ti	1.0	1.9	1.5

4.5. Temperature effects on the chlorate process

Temperature has an interesting effect on the main factors that determine the power consumption in the chlorate process. The oxygen formation, CCE and cell voltage vs. the temperature in the electrolyte are shown in Figure 4.18.

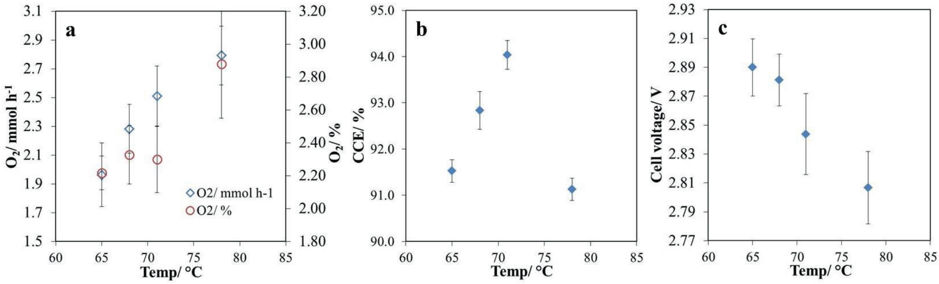

Figure 4.18 Measurements of oxygen formation (a), cathodic current efficiency (b) and cell voltage (c) in a sodium chlorate pilot unit after two weeks of operation. The electrolyte was 110 gdm^{-3} NaCl, 580 gdm^{-3} $NaClO_3$, and 5 gdm^{-3} $Na_2Cr_2O_7$, and the temperature varied between 65 and 78 °C (Paper IV).

The formation of oxygen increases almost linearly with increasing temperature, as shown in Figure 4.18 a. This behaviour follows the expected trend discussed by Hardee et al. [22]. Oxygen formation is related to the decomposition rate of the hypochlorous acid and increased water oxidation on the anode. As shown in Figure 4.18 b, CCE has a maximum in current efficiency at approximately 71 °C and decreases with both lower and higher temperatures. For the lower temperatures, the decrease in CCE might be due to higher concentrations of hypochlorite in the electrolyte due to lower chlorate formation rates, which results in the hypochlorite being able to participate in side reactions to a greater extent. At 78 °C, the decrease is proposed to be due to the ability of chlorate to oxidise the chromium (III) film [40]. This might result in a thinner chromium (III) film during operation, which leads to a lower CCE and promotes heavier corrosion when the power is shut down. As shown in Figure 4.18 c, the cell voltage presents opposite behaviour compared to oxygen formation, as it linearly decreases with increasing temperature. The temperature decreased the cell voltage at 8 mV°C^{-1} due to increased conductivity and reduced overpotentials.

4.6. Sulphate effects on the chlorate process

Adding sodium sulphate to the electrolyte, as shown in Figure 4.19 a, has a decreasing effect on the oxygen formation. This has recently been reported by Owe et al. [77, 78], who concluded that sulphate ions block the sites where oxygen is produced at iridium anodes. There have also been contradictory discussions in the literature about the effect of sulphate on oxygen formation [47, 79, 80].

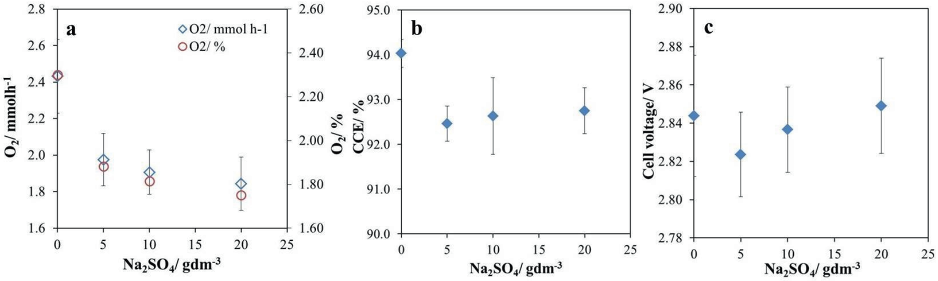

Figure 4.19 Measurements of oxygen formation (a), cathodic current efficiency (b) and cell voltage (c) in a sodium chlorate pilot unit after two weeks of operation. The electrolyte was 110 gdm^{-3} NaCl, 580 gdm^{-3} NaClO$_3$, and 5 gdm^{-3} Na$_2$Cr$_2$O$_7$ at 71 °C. Sodium sulphate was added at concentrations of 0, 5, 10 and 20 gdm^{-3} (Paper IV).

Sodium sulphate appears to have a binary effect on the CCE, as shown in Figure 4.18 c. With sulphate present in the electrolyte, there is a small decrease in current efficiency, but this decrease is not concentration dependent. There is no effect of sodium sulphate on the cell voltage. From the perspective of power consumption, the combined effect from having sulphate in the electrolyte appears insignificant.

4.7. Corrosion at the cathode

Corrosion of the mild steel cathodes significantly depends on the operating conditions in the sodium chlorate cell. In this investigation, the corrosion was evaluated depending on the dichromate concentration, temperature and sodium sulphate concentration. Although the cathodes were kept in the cells unpolarised for 40 minutes, the surface layers did not fully develop crystalline phases of Fe(III). The XRD patterns and IR spectra can be observed in Paper IV. Photographs taken of the surfaces provided a visual perception of the corrosion amounts and types, as shown in Figure 4.20.

The electrodes showing crystalline phases that were detectable using XRD are the bluish/green/grey samples presented in Figures 4.20 c, d, g and i. Some small peaks could also be found on the samples shown in Figures 4.20 h and l. These phases were two different types of green rust: green rust 1 (GR1) and green rust 2 (GR2). The type of green rust formed depends on the available counter ion, such as chloride or carbonate (GR1) and sulphate (GR2) [81]. Green rust is an intermediate mixed oxide of Fe(II) and Fe(III). The other electrodes show poorly crystalline phases, which clearly appear as the brown electrodes in Figures 4.20 a, b, e, f, h, j, k and l. This result may be an indication of ferrihydrite, a poorly crystalline hydrated oxyhydroxide of Fe(III), or exGR-Fe(III), which is an oxidised form of green rust. Ferrihydrite and exGR-Fe(III) can be further transformed into goethite or lepidocrocite depending on the conditions [51]. Figures 4.20 h and l differ from the others by showing both the green rust and the poorly crystalline Fe(III) species.

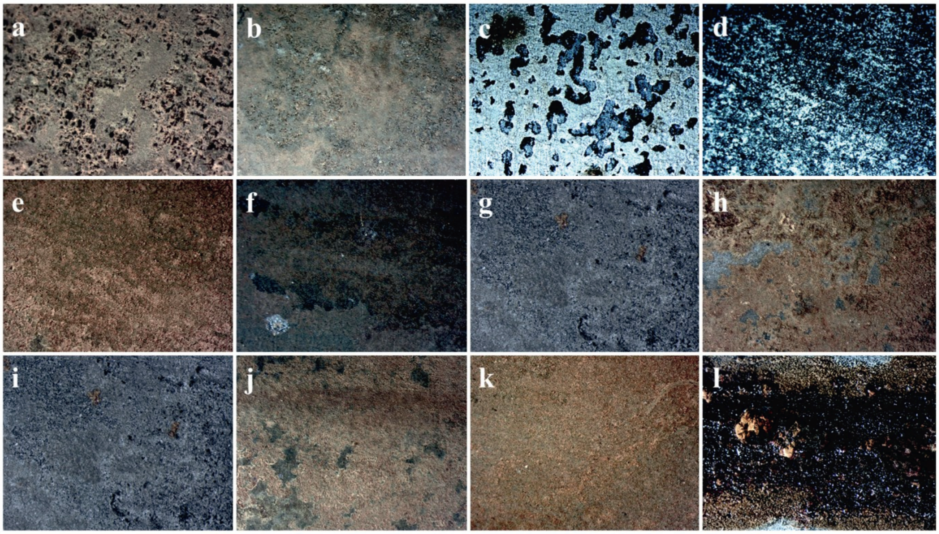

Figure 4.20 Photographs taken with an Olympus stereo microscope from the corroded mild steel cathodes used in the pilot plant with various operating conditions. The conditions in the top row were 1 gdm^{-3} (a), 3 gdm^{-3} (b), 5 gdm^{-3} (c) and 7 gdm^{-3} (d) of $Na_2Cr_2O_7$. In the second row, the conditions were 65 °C (e), 68 °C (f), 71 °C (g) and 78 °C (h). In the bottom row, the conditions were 0 gdm^{-3} (i), 5 gdm^{-3} (j), 10 gdm^{-3} (k) and 20 gdm^{-3} (l) of Na_2SO_4 (Paper IV)

The trials with different dichromate concentrations in the electrolyte are presented in row 1 in Figure 4.20. As shown, corrosion decreases with increasing concentration of dichromate. This result is visually observed from the pits and heavy corrosion in picture “a” with 1 gdm^{-3} to the almost clean surface from the trial with 7 gdm^{-3} in picture “d”, where the polishing grooves can still be observed. Lepidocrocite is also found on the surface from 1 gdm^{-3}. exGR-Fe(III) was observed on this surface as with 3 gdm^{-3}, whereas from 5 and 7 gdm^{-3}, GR1 and GR2 were found. The amount of corrosion depends on the chromate concentration in the electrolyte, i.e. is strongly related to the thickness of the mature chromium (III) film on the surface when the power is shut off.

The temperature dependence of the corrosion was studied, and photographs are presented in the second row. Poorly crystalline Fe(III) species such as exGR-Fe(III) were found in the samples exposed to 65, 68 and 78 °C, as shown in Figures 4.20 e, f, and h. Green rusts were found on the cathodes corroded at 71 and 78 °C. It is observed that the lowest and highest temperatures provided the heaviest corrosion (larger amounts of Fe(III)), whereas 71 °C showed the smallest corrosion (higher Fe(II) content). The decreased amount of Fe(III) with temperatures up to 71 °C might be related to, as previously discussed in Section 4.5, differences in the hypochlorite concentration that decrease with temperature, thus providing a less oxidising environment. At the highest temperature, the increased corrosion might be correlated to the ability of chlorate to oxidise trivalent chromium at elevated temperatures.

The investigation of the effect of sodium sulphates on corrosion is shown in the bottom row in Figure 4.20. The electrode tested at 71 °C (picture “g”) and with 0 gdm^{-3} (picture “a”) sodium sulphate is the same, showing a greyish to blue colour, and crystalline GR1 and GR2 were found. For the concentrations of 5 to 10 gdm^{-3} (pictures “j” and “k”) sodium sulphate, the colour was orange to dark brown, and exGR-Fe(III) was found. With 20 gdm^{-3} of sodium sulphate in the electrolyte (picture “l”), the worst visual appearance on the surface was obtained with uneven heavy corrosion. Despite the heavy visual corrosion, GR1 and GR2 were found on the surface together with exGR-Fe(III). The existence of Fe(II) in this sample might be explained by less oxidised surfaces being exposed when corrosion products fall off. The more sulphate there is in the electrolyte, the heavier the corrosion becomes on the surface.

The corrosion process on the chlorate cathode is interpreted as follows: the $Fe(OH)_2$ starts to oxidise by hypochlorite forming green rust, which is further oxidised to exGR-Fe(III), and finally, the Fe(III) is organised into α- or γ-FeOOH. The present study showed that green rust was surprisingly stable under these corrosive conditions as it was found as the sole oxidation product on several samples. The oxidation process has been proven to be strongly dependent on the operating conditions. However, there appears to be a time dependence on the crystallisation process from the amorphous Fe(III) to the well-ordered FeOOH species, which was not fully captured in this study. Notably, GR2 was found under conditions where sulphate was not present, indicating that another three-dimensional ion might be incorporated in the structure.

The corrosion increases with increasing sulphate concentration, decreases with increasing dichromate concentration and is minimised at approximately 71 °C.

5. Conclusions and recommendations

5.1. Conclusions

The present investigation showed that two cathodes taken from two full-scale sodium chlorate plants exhibit different performances upon start-up. It was observed that the poorly performing cathode had γ-FeOOH, lepidocrocite, on its surface, whereas the well performing cathode had α-FeOOH, goethite, on its surface. The poorly performing cathode started with zero current efficiency followed by a slow increase, whereas the well performing cathode had fairly high performance from the start. After more than 2 full days, the electrodes began to perform equally. A kinetic study of the hypochlorite reduction on the two different pure iron oxyhydroxide species could not explain the different behaviours of the two cathodes.

The two different iron oxyhydroxides both have high overpotentials for the HER, which are more than 300 mV higher than that for a freshly polished mild steel cathode. It was also observed that the trivalent iron was reduced to $Fe(OH)_2$, which is concluded to be the active species for hydrogen evolution on the chlorate cathode. The rate of the reduction of the two different FeOOH phases differed, where the reduction of γ-FeOOH starts at lower negative potentials compared to the α-FeOOH; however, at potentials where both species are reduced, it was observed that the α-FeOOH was more readily reduced. Therefore, a lower rate of hydrogen production with a subsequent low current efficiency will remain for a longer time during a start-up with a cathode covered with lepidocrocite, γ-FeOOH, than with a cathode covered with goethite, α-FeOOH.

The sodium dichromate added to the electrolyte has been proven to provide selectivity towards the HER irrespective of whether it is in the form of a trivalent chromium oxide or hydroxide. The selectivity cannot theoretically (according to DFT calculations) be attributed to its electrocatalytic properties. This result is interpreted to be the semiconducting properties that differentiate the Cr(III) from the Fe(III) species. This insight can be of great importance in the search for chemicals to replace sodium dichromate, which is listed under REACH Annex XIV.

The studies also show that increasing the dichromate concentration in the electrolyte increases the CCE along with the cell voltage. This is interpreted as increasing the thickness of the trivalent chromium film on the cathode leads to an increased selectivity for hydrogen evolution. An apparent optimum is assigned to 5 gdm^{-3} of $Na_2Cr_2O_7$ in the electrolyte. In addition, this oxygen formation, when measured as molar formation per time unit, has a linear decrease with increasing dichromate concentration in the electrolyte. This result shows that dichromate also has a positive effect on the chlorate formation reaction in the bulk, which also contributes to increasing the total current efficiency.

The performance of the chlorate cell was also influenced by temperature. The CCE increased with increasing temperature due to the increased rate of chlorate formation providing lower steady-state concentrations of hypochlorite. At the highest temperature, a dramatic decrease in the CCE was observed, which might be explained by the ability of chlorate to oxidise the outer layer of the trivalent chromium film, thereby decreasing the selectivity.

Sodium sulphate has minor effects on the performance of the chlorate cell. The addition of sodium sulphate decreases the CCE and increases the ACE without a concentration dependence.

The corrosion studies showed that the time for oxidation from $Fe(OH)_2$ to α-FeOOH or γ-FeOOH is significantly longer than expected in the corrosive electrolyte and that the chromium (III) film is not immediately oxidised. In several samples, the corrosion product was identified as green rust. Green rust is an intermediate phase that is a mixture of Fe(II) and Fe(III). Further oxidation of green rust yields the poorly crystalline trivalent iron exGR-Fe(III). The dichromate concentration in the electrolyte influences the oxidation state of the corrosion products formed on the surface. A corrosion product with a lower oxidation state (green rust) was found at the higher chromium concentrations, whereas the trivalent corrosion products were formed at lower chromium concentrations. The effect of temperature on the corrosion behaviour showed that the trivalent oxidation products were predominant at the lowest and highest temperatures, whereas green rust was observed at the intermediate temperatures. This result is interpreted as the electrodes being exposed to a more oxidising environment at lower temperatures due to the higher hypochlorite concentration. At the highest temperature, the oxidation of chromium (III) by chlorate becomes significant, which will remove the protective film and intensify the corrosion on the cathode. The corrosion is intensified with increasing concentration of sulphate in the electrolyte even though dichromate is present. Trivalent corrosion products were observed in all trials with sodium sulphate.

5.2. Recommendations for future work

The work conducted in this thesis is comprehensive but has left some questions that need to be answered. Future work would be successful if the following items are addressed:

- A kinetic study was performed on FeOOH phases with respect to chlorate reduction. This was not studied in this work due to a preliminary study on fresh mild steel cathodes showing slower or similar kinetics than for hydrogen evolution. For the sake of completeness and to address this question, the chlorate reduction should be studied.
- Development of techniques for *in situ* XRD, SEARS, XANES, EXAFS or neutron scattering to actually observe the $Fe(OH)_2$ would be beneficial for verification.
- Stops in the operation, where the electrodes are unpolarised, in the pilot plant needs to be considerably longer, as 40 minutes is not sufficient to study the corrosion phenomena. Some extended trials were performed with 2 hours stops, but even this time period did not fully oxidise the surface. Green rust and amorphous structures were still observed.
- Evaluate whether other p-type semiconductors also inhibit hypochlorite reduction to find alternatives for chromium.
- Study the chlorate formation reaction kinetics with respect to dichromate concentration and learn how it affects the rate.
- Develop the durability of the rotating disc electrodes and repeat the kinetic experiments at elevated temperatures and in strong electrolytes.

- Test whether chlorate can act as a counter anion in green rust 2. In some experiments, XRD peaks for green rust 2 are visible but no obvious counter ion, i.e. sulphate, is present on the surface.
- Use the pilot plant to follow in detail the current efficiency during start-up after shutdowns.

5.3. Recommendation for sodium chlorate producers

Every time a plant shuts down, i.e. the rectifiers are turned off, the cathodes lose their protective potential and begin to corrode. The loss of material from the cathode due to corrosion is significant, and the cathode only survives a limited number of shutdowns. However, the corrosion of the surface is not entirely negative; the surface can be renewed from deposits by the corrosion occurring during shutdowns. Such surface renewal can also be achieved during acid washes. It is shown that the cathode has an oxidised surface during operation that consists of $Fe(OH)_2$. This is regardless of whether it is a new cathode or an old and corroded cathode. The iron on the fresh surface will oxidise by the water, and the corroded cathode will be reduced during operation to form this species.

The shutdown procedure is extremely important. The cathode will corrode during shorter stops, less than 2 hours, however, the corrosion products will not fully develop into a crystalline trivalent structure. This is why a fast start-up and recovery of current efficiency can be retained. During longer shutdowns, different types of crystalline FeOOH develop, and the formation is strongly dependent on the process parameters in the plant and shutdown procedures. Two different forms of crystalline FeOOH have been identified on chlorate cathodes, and the start-up situation differs significantly depending on which one is formed on the cathode. In fact, it can take more than 50 hours from the start-up until the current efficiency is regained. To reach full current efficiency, steady-state operation, takes more than 100 hours. If the wrong form of FeOOH is formed, γ-FeOOH or lepidocrocite, the current efficiency is so poor that if nitrogen is not used to purge the cells during the first 30 hours, their might be explosive mixtures of hydrogen and oxygen in the cell gas leading to catastrophic events.

To avoid this situation, there are some steps that should be followed.

- Sodium dichromate is unfortunately a necessary process chemical. It is recommended to keep the concentration at a minimum of 5 gdm^{-3} to keep sufficient current efficiency and low corrosion.
- The optimum temperature range during operation and shutdown is between 71 and 78 °C. This is optimum from a corrosion perspective during shutdown and for current efficiency during operation.
- The recommendation is to minimise the intake of sodium sulphate to the greatest extent possible in order to reduce the corrosion.
- The last is also the most obvious: reduce the number of shutdowns! Since it takes up to 4 days to regain current efficiency and fully renew the active surface, it must be taken into consideration when running and stopping a chlorate plant.

Acknowledgements

In this work, I have had help from many contributors that I would like to acknowledge and thank. There is no dependence of the amount of gratitude on the order of appearance.

I would like to start by expressing my gratitude to the Swedish Energy Agency and their program “Effektivisering av industrins energianvändning” 33280-1 and AkzoNobel AB for funding this project. I will continue on the industrial path by thanking Permascand AB for supplying fresh electrodes and AkzoNobel Pulp and Performance Chemicals for the used electrodes that were used in this work. Additionally, BIS Production partner and their competent personnel located in Bohus have performed tremendous work in constructing and maintaining the pilot unit used.

My main supervisors, Elisabet Ahlberg from the University of Gothenburg and Nina Simic from AkzoNobel Pulp and Performance Chemicals together with my co-supervisor Mats Wildlock, also from AkzoNobel Pulp and Performance Chemicals, have with their vast competence given this project a scientific edge that I could have never achieved myself. They have also contributed significantly with the analysis and interpretation of the results in combination with the outstanding feedback during all the writing. I owe you big time for all the laughter’s, sweats and tears that went with this project!

At AkzoNobel Pulp and Performance Chemicals, I also wish to thank my project sponsors Kalle Pelin and Rolf Edvinsson-Albers, who have given me invaluable feedback and control over the time schedule.

At the start-up, I had a steering group that guided me from my vast and broad experiments to the right track from a scientific and industrial perspective. These members included Sture Nordholm at the University of Gothenburg, Ann Cornell at the Royal Institute of Technology in Stockholm, Magnus Karlsson from AkzoNobel Pulp and Performance Chemicals plant in Alby, Sweden, and Joakim Bäckström from Mid Sweden University. Joakim Bäckström also became a co-author on one paper because of his immense knowledge in Raman spectroscopy.

For the use of and help with the Raman spectroscopy experiments, I would like to acknowledge Aleksandar Matic and Ezio Zanghellini from the Physics department at Chalmers University of Technology.

Also from Chalmers, I would like to thank Vratislav Langer for help with the XRD measurements, Anders Kvist for the SEM and EDX analyses and finally Rikard Ylmèn for his knowledge in IR spectroscopy.

I send a special recognition to the man who “pulled” me down from Umeå to Gothenburg and taught me all that AkzoNobel knows about sodium chlorate, Johan Wanngård. He also helped considerably with the design and construction of the pilot unit.

Brecht Van Gastel performed his master´s thesis for me and taught me how to run the pilot unit with the most efficient experiments.

At the University of Gothenburg, I would like to thank both the electrochemistry group and physical chemistry group for fruitful discussions and seminars. A special gratitude is needed for “my partner in crime” Adriano Gomes, my office mate who bore with me Zareen Abbas, Michael Bush for the DFT calculations and Johanna Löberg for introducing me to the Ph.D. work.

At AkzoNobel Pulp and Performance Chemicals, Annicka Sellin, Jan Olov Johansson, Tobias Jonasson and Eie Carlberg have helped tremendously with the operation and maintenance of the pilot unit.

Many thanks to Andrea Boschin for all the laughs at lunch hours and beer nights when I needed time away from work.

The final but absolutely not the least gratitude goes to my family, who coped with me during the time and all weekends, holidays and vacations I have worked, Linda, Filippa and Sigrid Hedenstedt.

Bibliography

1. Vogt, H., et al., *Chlorine oxides and chlorine oxygen acids*, in *Ullman's Encyclopoedia of Industrial Chemistry*. 2010, Wiley-VCH Verlag GmbH & CO. KGaA.

2. Mendiratta, S.K. and B.L. Duncan, *Chloric Acid and Chlorates.* Kirk-Othmer Encyclopaedia of Chemical Technology, 2003. **6**: p. 111.

3. Cornell, A., *Chlorate Cathodes and Electrode Design*, in *Encyclopedia of Applied Electrochemsitry*, G. Kreysa, K.-i. Ota, and R. Savinell, Editors. 2014, Springer Reference. p. 175-181.

4. Bergnor, E. and P. Axegård. *Environmental Performance of Modern ECF-Bleaching*. in *International Pulp Bleaching Conference 2011 (IPBC 2011)*. 2011. Portland, Oregon: TAPPI press.

5. *Trends in World Bleached Chemical Pulp Production: 1990-2010* 2011 [cited 2016 2016-06-03].

6. *Best available techniques (BAT) reference document for the production of pulp, paper and board*, I.f.P.T. studies, S.P.a.C. Unit, and E.I. Bureau, Editors. 2015, European IPPC Bureau: http://eippcb.jrc.ec.europa.eu/. p. 900.

7. Barroca, M., et al., *Selectivity studies of oxygen and chlorine dioxide in the pre-delignification stages of a hardwood pulp bleaching plant.* Industrial & Engineering Chemistry Research, 2001. **40**: p. 5680-5685.

8. Müller, E., *Über ein elektrlytisches verfahren zur gewinnung der chlor-, brom- und jodsuren salze der alkalien.* Zeitschrift für Elektrochemie, 1899. **41**: p. 469-473.

9. Colman, J.E., *Electrolytic production of sodium chlorate.* AIChE Symposium Series, 1981. **77**: p. 244-263.

10. Beer, H.B., *Brittish Patent no. 1 195 871*1965. p. 1.

11. Wulff, J. and A. Cornell, *Cathodic current efficiency in the chlorate process.* Journal of Applied Electrochemistry, 2007. **37**: p. 181-186.

12. AkzoNobel, A., *A Chlorate Handbook*, in *BREF AkzoNobel information to customers*. 2005.

13. Viswanathan, K. and B.V. Tilak, *Chemical, electrochemical and technological aspects of sodium chlorate formation.* Journal of the Electrochemical Society, 1984. **131**(7): p. 1551-1559.

14. Landin, J., *SE-8820, Förfaringssätt vid framställning af klorater och perklorater*. 1897, Johan Landin: Sweden. p. 1.

15. Taniguchi, I. and T. Sekine, *The influence of chromate addition on the cathode reduction of hypochlorite ion.* Denki Kagaku, 1975. **43**: p. 201-208.

16. Lindbergh, G. and D. Simonsson, *The effect of chromate addition on cathodic rduction of hypochlorite in hydroxide and chlorate solutions.* Journal of the Electrochemical Society, 1990. **137**(10): p. 3094-3099.

17. Tilak, B.V. and C.-P. Chen, *Chlor-Alkali and Chlorate Technology*, in *The ElectrochemicalSociety Proceedings Series*. 1999: Pennington, NJ. p. 8.

18. Vogt, H., *Electrosyntesis of chlorate in the nineteenth century.* Journal of the Electrochemical Society, 1981. **128**(2): p. 23-32.

19. Foerster, F. and F. Jorre, *Zur Kentniss der beziehungen der unterchlorigsauren salze zu den chlorsauren salzen.* Journal der Praktische Chemie, 1899. **59**: p. 53-101.

20. Kotowskii, S., B. Busse, and K. Wall, *Modern Chlor-Alkali Technology*. 1986, Ellis Horwood Ltd.: Chichester. p. 310.

21. Tilak, B.V. and C.-P. Chen, *Calculation of the current efficiency of the electrolytic sodium chlorate cell.* Journal of Applied Electrochemistry, 1999. **29**: p. 1237-1240.

22. Hardee, K.L. and L.K. Mitchell, *The influence of electrolyte parameter on the percent oxygen evolved from a chlorate cell.* Journal of the Electrochemical Society, 1989. **136**(11): p. 3314-3318.

23. Cornell, A. and D. Simonsson, *Ruthenium Dioxide as Cathode Material for Hydrogen Evolution in Hydroxide and Chlorate Solutions.* Journal of the Electrochemical Society, 1993. **140**(11).

24. Edvinsson-Albers, R., K. Hedenstedt, and M. Rosvall, *WO2009063031 A3, Electrode*. 2009.

25. Schulz, R. and S. Savoie, *A newfamily of high performance nanostructured catalysts for the electrosynthesis of sodium chlorate.* Journal of alloys and compounds, 2009. **483**.

26. Schulz, R. and S. Savoie, *Properties of iron aluminide doped with a catalytic element for the electrosynthesis of sodium chlorate.* Journal of alloys and compounds, 2010. **504**.

27. Wagner, C., *Cathodic reduction of anions.* Journal of the Electrochemical Society, 1954. **101**(4): p. 180-184.

28. Spasojevic, M., N.V. Krstajic, and J.M. Jaksic, *Electrocatalytical optimization of faradaic yields in the chlorate cell process.* Surface technology, 1984. **21**: p. 19-26.

29. Jaksic, M., *Mutual effect of current density, pH, Temperature and hydrodynamic factors on current effeciency in the chlorate cell process.* Journal of the Electrochemical Society, 1974. **121**(1): p. 70-79.

30. Lindbergh, G. and D. Simonsson, *Inhibition of cathode reactions in sodium hydroxide solution containing chromate.* Electrochimica Acta, 1991. **36**(13): p. 1985-1994.

31. Ahlberg Tidblad, A. and G. Lindbergh, *Surface analysis with ESCA and GD-OES of the film formed by cathodic reduction of chromate.* Electrochimica Acta, 1991. **36**(10): p. 1605-1610.

32. Ahlberg Tidblad, A. and J. Mårtensson, *In Situ ellipsometric characterization of films formed by cathodic reduction of chromate.* Electrochimica Acta, 1996. **42**(3): p. 389-398.

33. Cornell, A., G. Lindbergh, and D. Simonsson, *The effect of addition of chromate on the hydrogen evolution reaction and on iron oxidation in hydroxide and chlorate solutions.* Electrochimica Acta, 1992. **37**(10): p. 1873-1881.

34. Cotton, F.A. and G. Wilkinson, *Advanced Inorganic Chemistry*. 5th ed. 1988, New York: John Wiley & Sons inc.

35. Neuss, J.D. and W. Riemann III, Journal American Chemical Society, 1934. **56**.

36. Mason, J.G. and A.D. Kowoalak, Inorganic Chemistry, 1964. **3**.

37. Brito, F., et al., *Equilibria of chromate(VI) species in acid medium and ab initio studies of these species.* Polyhedron, 1997. **16**(21): p. 3835-3846.

38. Svedin, B.H., B. Sundblad, and J. Engstrom, *Process for the production of chlorine dioxide*. 1991, Eka Nobel AB.

39. Cornell, A., B. Håkansson, and G. Lindbergh, *Ruthenium-Based Dimensionally Stable Anode in Chlorate Electrolysis: Effects of Electrolyte Composition on the Anode Potential.* Journal of The Electrochemical Society, 2003. **150**(1): p. D6-D12.

40. Hedenstedt, K. and R. Edvinsson Albers, *US 2013/0292261, Electrolytic Process*. 2013, Akzo Nobel Chemicals International B.V.

41. Commission, T.E., *Commission Regulation (EU) No 348/2013 of 17 April 2013 amending Annex XIV to Regulation (EC) No 1907/2006 of the European Parliament and of the Council on the Registration, Evaluation, Authorisation and Restriction of Chemicals (REACH) Text with EEA relevance*. 2013: http://data.europa.eu/eli/reg/2013/348/oj. p. 5.

42. Li, M., et al., *Sodium molybdate - a possible alternative additive for sodium dichromate in the electrolytic production of sodium chlorate.* Journal of Applied Electrochemistry, 2007. **37**: p. 499-507.

43. Rosvall, M., et al., *US2012/0061252, Activation of Cathode*. 2012, Akzo Nobel Chemicals International B.V.

44. Nylén, L., J. Gustavsson, and A. Cornell, *Cathodic Reactions on an Iron RDE in the presence of Y(III).* Journal of the Electrochemical Society, 2008. **155**(10): p. E136-E142.

45. Gustavsson, J., L. Nylén, and A. Cornell, *Rare earth metal salts as potential alternatives to Cr(VI) in the chlorate process.* Journal of AppliedElectrochemistry, 2010. **40**: p. 1529-1536.

46. Gustavsson, J., et al., *On the suppression of cathodic hypochlorite reduction by electrolyte additions of molybdate and chromate ions.* Journal of Electrochemical Science Engineering, 2012. **2**: p. 185-198.

47. Jaksic, M.M., et al., Journal of the Electrochemical Society, 1969. **116**.

48. Bragg, W.L. and H. Lipson, *Letters to the editor No. 3565.* Nature, 1938. **26**: p. 367.

49. Goldstein, G.I., et al., *Scanning electron microscopy an X-ray microanalysis*. 2003, New York: Springer Sciences + Buissiness Media.

50. Shimizu, K. and T. Mitani, *New Horizons of Applied Scanning Electron Microscopy*. 2010, Heidelberg: Springer.

51. Schwertmann, U. and R.M. Cornell, *Iron Oxides In The Laboratory*. Second ed. 2000, Weinheim: Wiley-VCH.

52. Levich, V.G., *Physiochemical Hydrodynamics*. 1962, New Jersey: Prentice Hall.

53. Bard, A.J. and L.R. Faulkner, *Electrochemical methods- Fundamentals and applications*. Second ed. 2001: John Wiley & Sons.

54. Newman, J. and K.E. Thomas-Alyea, *Electrochemical Systems*. Third ed. 2004, Hoboken, New Jersey: John Wiley & Sons, Inc.

55. Ahlberg, E. and H. Anderson, *Simulating impedance spectra from a mechanistic point of view: Theory and simulations.* Acta Chemica Scandinavica, 1992. **46**: p. 1-14.

56. Martinez, L., et al., *Electrochemical growth of diverse iron oxide (Fe3O4, a-FeOOH, and y-FeOOH) Thin films by electrodeposition potential tuning.* Journal of the Electrochemical Society, 2007. **154**(3): p. D126-D133.

57. Aguilar, M., et al., *Characterization of black and white chromium electrodeposition films: surface and optical properties.* Journal of Non-Crystalline Solids, 2003. **329**: p. 31-38.

58. Cornell, A., *Chlorate Synthesis Cells and Technology*, in *Encyclopedia of Applied Electrochemistry*, G. Kreysa, K.-i. Ota, and R. Savinell, Editors. 2014, Springer Reference. p. 181-187.

59. Landolt, D. and N. Ibl, *On the mechanism of anodic chlorate formation in concentrated NaCl solutions.* Electrochimica Acta, 1970. **15**(7): p. 1165-1183.

60. *Energy Price Statistics*. 2016-07-25 [cited 2016 2016-08-16]; Available from: http://ec.europa.eu/eurostat/statistics-explained/index.php/Energy_price_statistics#Electricity_prices_for_industrial_consumers.

61. Monnier, J., et al., *ZAS and XRD in situ characterisation of reduction and reoxidation processes of iron corrosion products involved in atmospheric corrosion.* Corrosion Science, 2014. **78**: p. 293-303.

62. Beverskog, B. and I. Puigdomenech, *Revised Pourbaix diagrams for iron at 25-300°C.* Corrosion Science, 1996. **38**(12): p. 2121-2135.

63. Cohen, M. and K. Hashimoto, *The cathodic reduction of y-FeOOH, y-Fe2O3, and oxide films on iron.* Journal of the Electrochemical Society, 1974. **121**(1): p. 42-45.

64. Stratmann, M., K. Bohenkamp, and H.-J. Engell, *An electrochemical study of phase-transitions in rust layers.* Corrosion Science, 1983. **23**: p. 969-985.

65. Antony, H., et al., *Study of lepidocrocite γ–FeOOH electrochemical reduction in neutral and slightly alakaline solutions at 25 °C.* Electrochimica Acta, 2005. **51**: p. 745-753.

66. Jolivet, J.P., C. Chaneac, and E. Tronc, *Iron oxide chemistry. From molecular clusters to extended solid networks.* Chem Commun (Camb), 2004(5): p. 481-7.

67. Baes, C.F.J. and R.E. Mesmer, *The Hydrolysis of Cations*. 1976, New York: John Wiley & Sons, Inc.

68. Odziemkowski, M.S., et al., *Mechanism of oxide film formation on iron in simulating groundwater solutions: Raman spectroscopic studies.* Corr. Sci., 1998. **40**(2/3): p. 371-389.

69. Lutz, H.D., H. Möller, and M. Schmidt, *Lattice vibration spectra. Part LXXXII. Brucite-type hydroxides M(OH)2 (M=Ca, Mn, Co, Fe, Cd) - IR and Raman spectra, neutron diffraction of Fe(OH)2.* Journal of Molecular Structure, 1994. **328**: p. 121-132.

70. de Faria, D.L.A., S. Venancio Silva, and M.T. de Oliveira, *Raman Microspectroscopy of Some Iron Oxides and Oxyhydroxides.* Journal of Raman Spectroscopy, 1997. **28**(873-878): p. 873.

71. Oblonsky, L.J. and T.M. Devine, *A surface enhanced Raman spectroscopic study of the passive films formed in Borate buffer on Iron, Nickel, Chromium and Stainless steel.* Corrosion Science, 1995. **37**(1): p. 17-41.

72. Asteman, H., E. Ahlberg, and J.-E. Svensson, *Electric properties of alpha-*Fe_2O_3*,* Cr_2O_3 *and alpha-*$(Cr,Fe)_2O_3$ *and their relevance to corrosion.* Electrochem. Soc., 2000. **99-38** p. 17 - 25.

73. Colman, J.E. and B.V. Tilak, *Sodium Chlorate*, in *Encyclopedia of Chemical Processing and Design*. 1995, Dekker: New York. p. 126-188.

74. Nylén, L. and A. Cornell, *Critical Anode Potential in the Chlorate Process.* Journal of The Electrochemical Society, 2006. **153**(1): p. D14-D20.

75. Sandin, S., R.K.B. Karlsson, and A. Cornell, *Catalyzed and Uncatalyzed Decomposition of Hypochlorite in Dilute Solutions.* Industrial & Engineering Chemistry Research, 2015. **54**(15): p. 3767-3774.

76. Wanngård, J., *The catalyzing effect of chromate in the chlorate formation reaction.* Chemical Engineering Research and Design, 2017. **In Press**.

77. Owe, L.-E., et al., *Electrochemical Behavior of Iridium Oxide Films in Trifluoromethanesulfonic Acid.* Journal of The Electrochemical Society, 2010. **157**(11): p. B1719-B1725.

78. Owe, L.-E., M. Tsypkin, and S. Sunde, *The effect of phosphate on iridium oxide electrochemistry.* Electrochimica Acta, 2011. **58**: p. 231-237.

79. Bondar, R.U., A.A. Borisova, and E.A. Kalinovskii, *Titanium-Ruthenium dioxide anodes in the electrolysis of chloride - sulfate solutions.* Elektrokhimiya, 1974. **10**(1): p. 44-48.

80. Buné, N.Y., et al., *Effect of foreign anions on the kinetics of chlorine and oxygen evolution on Ruthenium-Titanium oxide anodes under the conditions of chlorine electrolysis.* Elektrokhimiya, 1984. **20**(10): p. 1193-1197.

81. Génin, J.-M.R., et al., *Thermodynamic Equilibria in Aqueous Suspensions of Synthetic and Natural Fe(II)−Fe(III) Green Rusts: Occurrences of the Mineral in Hydromorphic Soils.* Environmental Science & Technology, 1998. **32**(8): p. 1058-1068.